Journal of Petrology, 2024, **65**, egae018
https://doi.org/10.1093/petrology/egae018
Advance access publication date 29 February 2024
Original Manuscript

Genesis of Andesitic Magma Erupted at Yufu Volcano, Kyushu Island, Southwest Japan Arc: Evidence from the Chemical Compositions of Amphibole Phenocrysts

Ikuo Okada[1,2,3,*], Tomoyuki Shibata[1,2], Masako Yoshikawa[1,2], Hidemi Ishibashi[4], Takeshi Sugimoto[5] and Yasutaka Hayasaka[1,2]

[1]Earth and Planetary Systems Science Program, Graduate School of Advanced Science and Engineering, Hiroshima University, 1-3-1, Kagamiyama,Higashihiroshima, Hiroshima 739-8526, Japan
[2]Hiroshima Institute of Plate Convergence Region Research, 1-3-1, Kagamiyama, Higashihiroshima, Hiroshima 739-8526, Japan
[3]Geological Survey Japan, AIST, Tsukuba Central 7, 1-1-1 Higashi, Tsukuba, Ibaraki 305-8567, Japan
[4]Department of Geoscience, Faculty of Science, Shizuoka University, 836 Ohya, Suruga-ku, Shizuoka, Shizuoka 422-8529, Japan
[5]Geothermal Engineering Co., Ltd, 356-6, Ogamaoshimizu, Takizawa, Iwate 020-0758, Japan

[*]Corresponding author. Telephone: +81-824-24-7469. E-mail: ikuo.okadageo@gmail.com

The major- and trace-element compositions of amphiboles in andesite from Quaternary Yufu Volcano, northeastern Kyushu, Japan were analysed to investigate the generation processes of andesitic magma from Yufu Volcano. The amphiboles in andesite from Yufu volcano can be divided into two groups based on major-element composition: pargasite and magnesio-hornblende. To estimate temperature, pressure, and major- and trace-element compositions of melts in equilibrium with amphiboles, we used the recently proposed methods that can calculate temperature, pressure, major element compositions, and partition coefficients of trace-element between amphibole and melt using only the major-element compositions of amphibole. The estimated temperature, pressure, and major-element composition of melt in equilibrium with the amphibole phenocrysts indicate that each group crystallised under different conditions. These differences suggest that two magma chambers at different depths existed beneath Yufu Volcano and that the andesitic magma of Yufu Volcano was formed by mixing of the two magmas. The trace-element compositions of melts in equilibrium with the pargasite and magnesio-hornblende, estimated by applying the partition coefficients calculated from major-element compositions of amphibole to trace-element compositions of amphiboles, indicate magma derived from slab melt and the partial melting of crustal material, respectively. Because magma is a mixture of minerals and melt, we estimate the chemical compositional ranges of the two end-member magmas on the Y versus SiO_2 diagram from the mixing relationship between amphibole and estimated melt, as well as phenocrysts of plagioclase, clinopyroxene, and orthopyroxene. The overlap of the estimated compositional range with the trend of whole-rock composition represents the chemical compositions of the end-members of magma mixing, yielding estimates of the mafic ($SiO_2 \approx 45$ wt %) and felsic ($SiO_2 \approx 68$ wt %) end-member magmas. Furthermore, we estimate the concentrations of other elements in the end-member magmas by substituting the estimated SiO_2 concentrations of the magmas into linear regression equations between the whole-rock contents of other elements and SiO_2. The trace-element compositions of the mafic and felsic end-member magmas, as estimated in this study, have similar features to those of gabbroids and Cretaceous granitic rocks, respectively, that are presumed to lie beneath Yufu Volcano. These similarities could be explained by the possibility that the compositions of the end-member magmas were influenced by basement rocks.

Key words: amphibole; andesite; magma mixing; trace-element; Yufu Volcano

INTRODUCTION

Although many early studies of the genesis and evolution of magma, especially basaltic magma, were developed under assumption that the magma keeps physicochemical equilibrium as a whole-rock, and is differentiated by fractional crystallisation (e.g. Kuno, 1968; Stern, 1979), it has also been recognised for many decades that magma mixing is one of the important processes to generate andesitic and other magmas, on the bases of disequilibrium mineral assemblages, mineral zoning, mafic inclusions, banded lava/pumice (e.g. Eichelberger, 1975, 1978; Sakuyama, 1979, 1981; Davidson & Tepley, 1997; Eichelberger *et al.*, 2006; Pichavant *et al.*, 2007; Kent *et al.*, 2010; Kent, 2014). Furthermore, DePaolo (1981) emphasised that crustal materials are incorporated into andesite magma on the basis of Sr isotopic study. These heterogeneities indicate that it is difficult to apply physicochemical equilibrium to andesitic magma, and this prevents us from characterising the primary magmas before magma mixing and crustal contaminations, and elucidating the origin and evolutionary processes of andesite from whole-rock geochemical composition (Tepley *et al.*, 2000; Eichelberger *et al.*, 2006; Pichavant *et al.*, 2007; Kent *et al.*, 2010; Kent, 2014).

To resolve these problems, melt inclusions, which are trapped in phenocrysts during crystal growth (Roedder, 1979), have used for various studies, such as physicochemical conditions of magma chamber and magma evolution processes (e.g. Anderson *et al.*, 1989; Saito *et al.*, 2001; Reubi & Blundy, 2009). However, melt inclusions are typically small and limited in the amount that can be analysed. In contrast, phenocryst in volcanic rocks also records the physicochemical information of the magma at the time of their crystallisation and is larger and more abundant

Received: November 27, 2022. **Revised:** January 15, 2024. **Accepted:** February 17, 2024

than melt inclusion. Thus, they have the advantage of providing more analytical data. The composition of amphiboles, which are common mineral in igneous rocks, changes during crystallisation with changing physicochemical conditions of the magma (e.g. Putirka, 2016; Zhang *et al.*, 2017), and contains a broad range of trace-elements (Tiepolo *et al.*, 2007). From these properties of amphiboles, Tiepolo *et al.* (2007) pointed out that amphiboles play an important role in understanding of lithospheric processes. It was suggested that many arc magma are residual after cryptic amphibole fractionation, and that the amphibole-rich cumulate can be implied the worldwide occurrence and the 'hidden' amphibole reservoir (e.g. Davidson *et al.*, 2007). Tiepolo *et al.* (2011, 2012) argued they have demonstrated above suggestions based on the major- and trace-element compositions of amphiboles in amphibole-rich intrusive rocks from Adamello batholith, Italy and Shikanoshima Island, Japan, which are considered to be the counterparts of extrusive rocks (high-Mg andesite). These studies indicate that the amphibole phenocrysts are a potential source of information about magma generation and evolution. Recently, the multivariate analyses of published high-*P*–*T* experimental data obtained under various *P*, *T*, and melt compositions have described the relationships between the major-element composition of individual crystals of amphibole and the *P*–*T* conditions of amphibole crystallisation (e.g. Ridolfi & Renzulli, 2012; Putirka, 2016; Ridolfi, 2021). Additionally, the major-element compositions of melt in equilibrium with amphibole, which have been determined mainly on the basis of the equilibrium with melt inclusion and matrix glass (e.g. Rutherford & Devine, 1988; Chertkoff & Gardner, 2004; Holtz *et al.*, 2005; Cooper & Wilson, 2014), can also be estimated from major-element compositions of individual amphibole by multivariate analysis of published data of high-*P*–*T* experiments (e.g. Ridolfi & Renzulli, 2012; Putirka, 2016; Zhang *et al.*, 2017). Many studies have applied these methods to natural samples to understand the physicochemical properties of magma (e.g. Turner *et al.*, 2013; Erdmann *et al.*, 2014; Nagasaki *et al.*, 2017; Ishibashi *et al.*, 2018; Okada *et al.*, 2018; Wanke *et al.*, 2019; Werts *et al.*, 2020). Moreover, the *Kd*s of trace-elements between amphibole and melt have been formulated as a function of *T*, and the major-element compositions of amphibole and melt have been determined by multivariate analysis of published datasets of high-P–*T* experiments (Shimizu *et al.*, 2017; Humphreys *et al.*, 2019). These studies allow us to determine *Kd*s according to the conditions of amphibole crystallisation by using the major-element compositions of amphibole that correlate with *T*, *P*, and melt composition. Furthermore, the methods of Shimizu *et al.* (2017) and Humphreys *et al.* (2019) can be used to estimate the *Kd*s of all rare earth elements (REEs) and Y, and 16 elements (Rb, Sr, Pb, Zr, Nb, some REEs, and Y), respectively. Therefore, for each amphibole crystal for which major- and trace-element data are available, it is possible to constrain the trace-element composition of melt in equilibrium with the amphibole.

Here, we report the major- and trace-element compositions of amphibole in andesite collected from the Yufu Summit lava of Yufu Volcano, which is a Quaternary volcano on the volcanic front of the Southwest Japan arc (Fig. 1). By applying the major-element compositions of amphiboles to the methods proposed from the multivariate analysis of published high-*P*–*T* experiment data, we estimate the *P*–*T* conditions and major-element compositions of melts in equilibrium with amphibole, and *Kd*s of trace-element between amphibole and melt. We also combine the calculated *Kd*s and trace-element compositions of amphibole to estimate the trace-element compositions of the melts that equilibrated with amphibole. Based on these estimated results, we infer the geochemical characteristics of the end-member magmas, and discuss the evolution process of andesitic magma from Yufu Volcano.

GEOLOGICAL BACKGROUND

Yufu Volcano is located in the Beppu–Shimabara graben of northeastern Kyushu, Japan, where the Philippine Sea Plate (PSP) is subducting beneath the Eurasian Plate (Fig. 1). Cretaceous granitic rocks are presumed to be widespread in the graben, but most are covered by younger volcanic rocks (Hoshizumi *et al.*, 1988; Matsumoto, 1993). The volcanic activity of Yufu Volcano began at ∼60 ka and has been characterised by repeated eruptions of lavas and pyroclastic flows until the latest activity at 2.2 ka (Kobayashi, 1984; Hoshizumi *et al.*, 1988; Ohta *et al.*, 1990). In terms of geology and stratigraphy, Ohta *et al.* (1990) divided the volcanic products from Yufu Volcano into early and late stages, with Kikai–Akahoya volcanic ash used as a widespread tephra layer with an age value of ca. 7.3 ka (Machida & Arai, 2003) as the boundary, and further subdivided the products into nine units (Fig. 1c). Of these, the units of the early stage are the Yufu main body lava, Yunotsubo lava, Sadohara lava, Kitainoseto lava, Imorigashiro lava dome, and Hyuugadake lava dome. The late stage comprises the Ikeshiro lava, Tsukahara lava, and Yufu Summit lava. The volcanic rocks of Yufu Volcano are andesite with plagioclase and amphibole [pargasite (Prg) and magnesio-hornblende (Mhb)] as major phenocryst, with clinopyroxene, orthopyroxene, opaque minerals, olivine, biotite, and quartz as subordinate phenocrysts (e.g. Ohta *et al.*, 1990). From the early to late stage, the whole-rock compositions become more mafic and there is an increase in the abundance of mafic inclusions and the clinopyroxene (Ohta *et al.*, 1990). The genesis of andesitic magmas from Yufu Volcano has been interpreted in terms of magma mixing on the basis of the following observations: 1) disequilibrium mineral assemblages such as olivine and quartz, anorthite-rich and anorthite-poor plagioclase, Prg and Mhb, and Mg-rich clinopyroxene and Mg-poor orthopyroxene (Fig. 2a, b); 2) linear variations in whole-rock major- and trace-element contents within a given range of SiO_2 content; and 3) a positive relationship between whole-rock Sr isotopic ratios and SiO_2 contents (Ohta *et al.*, 1990; Ohta & Aoki, 1991). Moreover, Ohta & Aoki (1991) assumed that the mixing end-members were represented by mafic inclusions in andesite from Yufu Volcano and dacite from an adjacent older volcano (Jissoji Volcano). Furthermore, some andesites from Yufu Volcano originate from adakitic magma derived from the partial melting of the subducting slab (Sugimoto *et al.*, 2006). On the major-element compositions of amphibole, Okada *et al.* (2018) applied them in Imorigashiro lava (Fig. 1c) to the geothermometer (Putirka, 2016), the barometer (Ridolfi & Renzulli, 2012) and the equation for estimating SiO_2 contents of melt in equilibrium with amphibole (Putirka, 2016), following Nagasaki *et al.* (2017). From the analysed major-element compositions of amphiboles in Imorigashiro lava and estimated *T*, *P* and SiO_2 contents of melt in equilibrium with amphibole, these authors inferred the following: 1) two types of amphibole crystallised from a mafic magma reservoir filled by andesitic melt at 940°C to 1000°C and 356 to 654 MPa (14–25 km depth), and a felsic magma reservoir filled by rhyolitic melt at 800°C to 840°C and 131 to 188 MPa (5–7 km depth); and 2) mixing of the magmas led to the coexistence of two types of amphibole in the andesite. However, the nature of the two magmatic end-members is poorly constrained.

In this study, we focus on the Yufu Summit lava, which is the lava most recently erupted from the summit and flowed on a

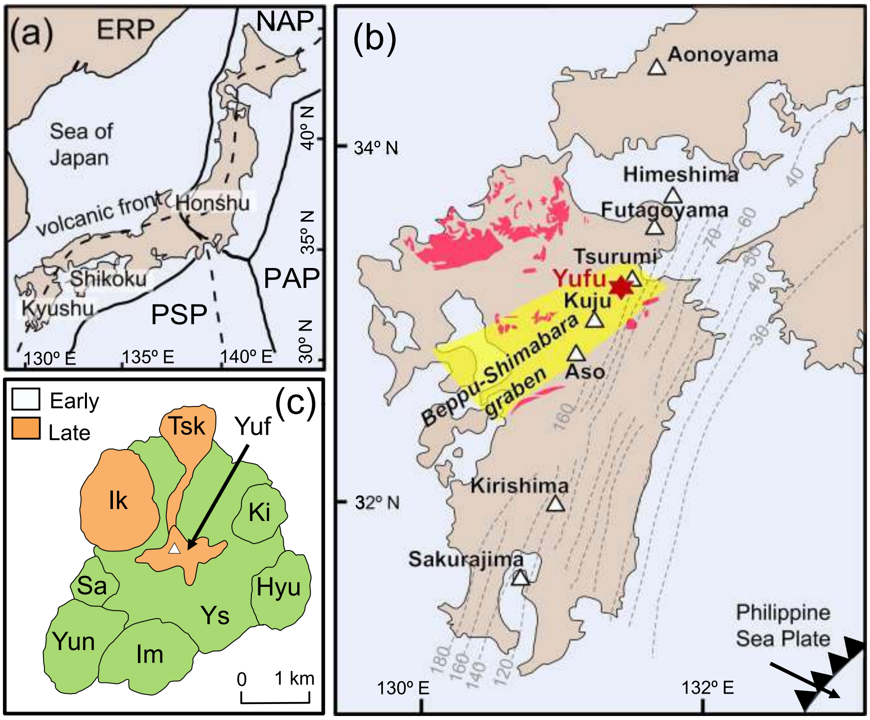

Fig. 1. Geological background. (a) Tectonic map of Japan, (b) map showing the distribution of Quaternary volcanoes of the Southwest Japan arc, and (c) simplified geological map of Yufu Volcano. The maps are modified after Shibata *et al.* (2014) and Sugimoto *et al.* (2006). PAP, PSP, ERP, and NAP denote the Pacific Plate, Philippine Sea Plate, Eurasian Plate, and North American Plate, respectively. Dashed lines in (a) and (b) are the volcanic front and isodepth contours of the upper boundary of the PSP, respectively. The hexagram and open triangles in (b) indicate the locations of Yufu Volcano and other Quaternary volcanoes, respectively. The yellow and pink shading in (b) depicts regions of the Beppu–Shimabara graben and Cretaceous granitic rocks, respectively (modified after Mahony *et al.*, 2011 and Kamei *et al.*, 2009, respectively). The lava units (from oldest to youngest) of the Yufu main body lava (Ys), Yunotsubo lava (Yun), Sadohara lava (Sa), Kitainoseto lava (Ki), Imorigashiro lava dome (Im), Hyuugadake lava dome (Hyu), Ikeshiro lava (Ik), Tsukahara lava (Tsk), and Yufu Summit lava (Yuf) are from Ohta *et al.* (1990). Units Ys to Hyu are early-stage lavas, and units Ik to Yuf are late-stage lavas. The boundary between the early and late stages is Kikai–Akahoya volcanic ash (ca. 7.3 ka; Machida & Arai, 2003).

small scale (Hoshizumi *et al.*, 1988; Ohta *et al.*, 1990). Sugimoto *et al.* (2006) reported that the Yufu Summit lava has the highest Sr/Y and lowest $^{87}Sr/^{86}Sr$ ratios (42 and 0.703892, respectively) of volcanic rocks from Yufu Volcano, which are within the range of adakite (>20 and <0.7040, respectively; Defant & Drummond, 1990, 1993).

METHODS

Analytical methods

Major-element compositions of amphiboles were analysed by electron probe micro-analyser (EPMA; JEOL JXA-8200®) at the Natural Science Centre for Basic Research and Development, Hiroshima University, Japan. The operating conditions were a 15 kV accelerating voltage, 10 nA beam current, and 3 μm beam diameter. The ZAF method was used for matrix corrections. The synthetic standards were used: jadeite for Si and Na, TiO_2 for Ti, Al_2O_3 for Al, Fe_2O_3 for Fe, MnO for Mn, Cr_2O_3 for Cr, MgO for Mg, wollastonite for Ca, and $KTiOPO_4$ for K. The analytical error (1 s) estimated from uncertainties outputted EPMA for each analysis were <0.17 wt % for SiO_2, <0.06 wt % for TiO_2, <0.10 wt % for Al_2O_3, and CaO, <0.12 wt % for FeO and MgO, <0.04 wt % for MnO, <0.03 wt % for Cr_2O_3 and K_2O, and <0.07 wt % for Na_2O.

Trace-element analyses of amphibole were conducted using laser ablation (LA)– inductively coupled plasma (ICP)–mass spectrometry (MS) on the same points as used for major-element analyses. A 213 nm Nd-YAG laser system (New Wave Research UP-213®) was connected to a Thermo Scientific X2 Series® Quadrupole ICP–MS instrument housed at the Earth and Planetary Systems Science facility, Hiroshima University. All analysis spots were located over EPMA spots and ablated for 30 s with a beam diameter of 40 μm, a repetition rate of 10 Hz, and a beam energy of 2.2 to 2.6 J/cm^2. Helium was used as a carrier gas to transport the ablated material from the ablation cell and was merged with Ar gas and N_2 gas at the outlet of the ablation cell. Trace-element abundances were calibrated using the standard glass NIST 610, with ^{43}Ca as the internal standard. Values for the standard glass NIST 610 were taken from Jochum *et al.* (2011), and CaO contents were determined by EPMA before LA–ICP–MS analysis. The precision and accuracy of the trace-element analyses were assessed by repeated measurements of the standard glass NIST 612, with results yielding relative standard deviations (RSDs) of <6% (1 s) for all elements and accuracies within ±8% of published values (Jochum *et al.*, 2011) (Supplementary Table 1).

Major- and trace-element (Rb, Ba, Sr, Zr, and Nb) contents of whole-rocks were determined using a RIGAKU 3070 X-ray fluorescence system, employing glass-bead and pressed-pellet methods, respectively. The procedures and instrumental set-up followed Sugimoto *et al.* (2006). The repeated measurement of BCR-3 and AGV-2 prepared by United States Geological Survey obtained the RSD of <0.6% (1 s), with the exception of MnO for AGV-2 (1.2%) (Supplementary Table 2). Trace-elements of whole-rocks were analysed using a VG Elemental PQ3® and Thermo Scientific X2 Series® quadrupole ICP–MS instrument installed at the Institute for Geothermal Sciences, Kyoto University, Japan. The analytical procedures and protocol were followed by Chang *et al.* (2003). The analytical reproducibility for each element was determined by repeated analyses of the JB-2 and JB-3 rock powder

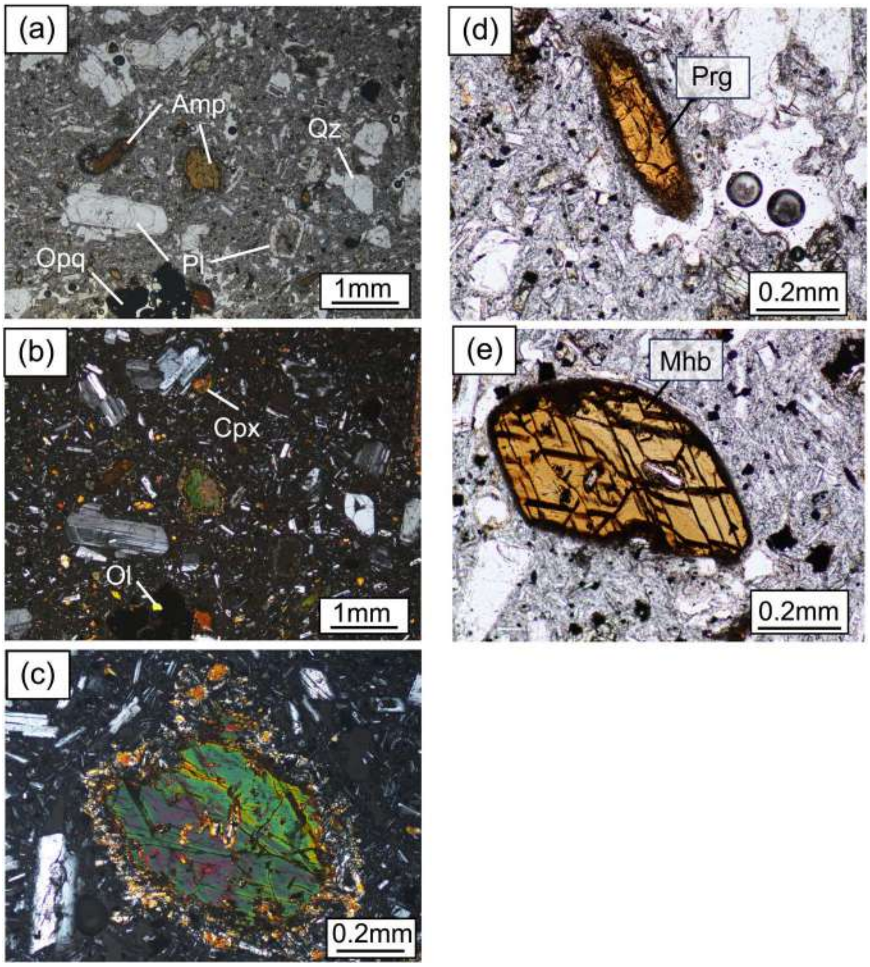

Fig 2. Photographs of sample from Yufu Summit lava. (a) and (b) thin section under open nicol and crossed nicol, respectively, and (c) amphibole phenocryst with reaction rim composed of pyroxene under crossed nicol. (d) and (e) pargasite (Prg) and magnesio-hornblende (Mhb), respectively. Mineral abbreviations are as follows: Pl, plagioclase; Amp, amphibole; Cpx, clinopyroxene; Ol, olivine; Qz, quartz; Opq; opaque.

(an international reference material from the Geological Survey of Japan), which yielded RSDs of <3% (1 s), with the exception of Y (5%) (Supplementary Table 3).

Estimation of amphibole crystallisation conditions

Following Nagasaki *et al.* (2017), we used the geothermometer of Putirka (2016) and the geobarometer of Ridolfi & Renzulli (2012) to estimate the *T* and *P* of amphibole crystallisation, respectively. For the estimation of crystallisation *P*, we also used the geobarometer of Ridolfi (2021). The geothermometer of Putirka (2016) is based on the number of cations of Si, Ti, Fe, and Na in amphibole when calculated on the basis of 23 atoms. Fe is the total iron as Fe^{2+}. The estimation error of the geothermometer proposed by Putirka (2016) is ±30°C. Ridolfi & Renzulli (2012) proposed the five equations calibrated under different *P* ranges (P1a,130–2200 MPa; P1b and P1c, 130–500 MPa; P1d, 400–1500 MPa; P1e, 930–2200 MPa). Similar to Erdmann *et al.* (2014) and Nagasaki *et al.* (2017), we used the average value of *P* obtained from P1b and P1c. The geobarometer of Ridolfi & Renzulli (2012) uses the number of cations of eight elements (Si, Ti, Al, Fe, Mg, Ca Na, and K), calculated using the sum of cations of elements (excluding Ca, Na, and K) as 13 (Leake *et al.*, 1997), as a variable. Fe is the total iron as Fe^{2+} as well. The geobarometer of Ridolfi (2021) is update version of Ridolfi & Renzulli (2012). Ridolfi (2021) proposed the new algorithms to determine the final *P* from different values obtained from the five equations of Ridolfi & Renzulli (2012), and added the compositional filter of amphibole for applying this new algorithms. In this study, the geobarometer of Ridolfi (2021) was performed using the Python3 tool Thermobar (v1.0.31, Wieser *et al.*, 2022). Furthermore, data that failed to pass the compositional filter of amphibole of Ridolfi (2021) were discarded. The reliability of geobarometers of Ridolfi & Renzulli (2012) and Ridolfi (2021) has been evaluated in several studies (e.g. Erdmann *et al.*, 2014; Putirka, 2016; Nagasaki *et al.*, 2017; Wieser *et al.*, 2023). According to Nagasaki *et al.* (2017), the geobarometer of Ridolfi & Renzulli (2012) can estimate *P* within ±85 MPa for cases where the SiO_2 content and *P* of melt equilibrated with amphibole are >60 wt % and 150 to 500 MPa, respectively. For the geobarometer of Ridolfi (2021), a root mean square error of ±270 MPa were yielded from tests using the experiment data not used for calibration of this geobarometer (Wieser *et al.*, 2023).

Several studies have proposed methods for estimating the major-element composition of melt in equilibrium with amphibole (Ridolfi & Renzulli, 2012; Putirka, 2016; Zhang *et al.*, 2017). The method of Putirka (2016) can estimate SiO_2 content and FeO*/MgO ratios, where FeO* is total iron oxides. Ridolfi & Renzulli (2012) and Zhang *et al.* (2017) proposed a series of equations for calculating the contents of SiO_2, TiO_2, Al_2O_3, FeO, MgO, CaO, and K_2O in melt in equilibrium with amphibole. In this study, to investigate in detail the geochemical characteristics of melt in equilibrium with amphibole, we used the equations of Zhang *et al.* (2017) for two main reasons. First, the equations of Ridolfi & Renzulli (2012) are given as a function of the *P* of amphibole crystallisation and the major-element content of amphibole. However, the exact *P* is unknown in our case. Second, Zhang *et al.* (2017) proposed equations using only the major-element composition of amphibole as a function, and improved the accuracy compared with the approach of Ridolfi & Renzulli (2012). To estimate SiO_2, TiO_2, FeO, MgO, CaO, K_2O and Al_2O_3 of melt in equilibrium with amphiboles, we selected equations (1), (6), (7), (9), (11), (12) and (14) from Zhang *et al.* (2017), respectively. These equations use the number of cations of Si, octahedral Al, Fe^{3+}, Mg, Ti, Fe^{2+}, Ca, and Na in A site, determined on the basis of the average Fe^{3+} model of Leake *et al.* (1997), as variable. The estimation errors are ±3.29 wt % for SiO_2, ±0.66 wt % for TiO_2, ±1.67 wt % for FeO, ±0.96 wt % for MgO, ±1.31 wt % for CaO, ±0.59 wt % for K_2O, and ±0.93 wt % for Al_2O_3 (Zhang *et al.*, 2017).

Calculation of partition coefficients

In this study, to estimate the trace-element composition of melt in equilibrium with individual amphibole crystals, we calculated the *Kd*s for each grain of amphibole using the method of Shimizu *et al.* (2017) for REEs and Y, and that of Humphreys *et al.* (2019) for Rb, Nb, Pb, Sr, and Zr. Humphreys *et al.* (2019) also proposed equations for calculating the *Kd*s of some REEs (excluding Pr, Tb, Tm, and Er) and Y. In contrast, the method of Shimizu *et al.* (2017) can be used to calculate the *Kd*s of all REEs and Y. Moreover, the partitioning behaviour of REEs and Y between amphibole and melt can be quantitatively described by the lattice strain model (Blundy & Wood, 1994; Shimizu *et al.*, 2017). Shimizu *et al.* (2017) parameterised the lattice strain model as a function of *T* and major-element compositions of amphibole. Therefore, adopting the method of Shimizu *et al.* (2017) should enable an estimation of the concentration of REEs and Y of melt in equilibrium with amphibole. The amphibole compositions required for this method are the number of cations of Ti, Mg, Na and K in amphibole per 23 oxygens, and the sum of Fe^{2+}, Mn^{2+}, and Mg in the M4 site assuming that all Fe is ferrous (Shimizu *et al.*, 2017). *T* were used the results obtained from the geothermometer of Putirka (2016). This method can reproduce the *Kd*s determined in high-*P*–*T* experiments within the range of 0.5 to 2 times (Shimizu *et al.*, 2017).

Humphreys *et al.* (2019) developed equations to calculate *Kd*s of Rb, Nb, Pb, Sr, and Zr, which cannot be calculated using the method of Shimizu *et al.* (2017). In this study, to determine the concentration of Rb, Nb, Pb, Sr, and Zr of melt in equilibrium with amphibole, we calculated *Kd*s of these elements using the equations (1)–(5) from Humphreys *et al.* (2019). These equations use the cations of Si, octahedral Al, Fe^{3+}, Mg, Ti, Fe^{2+}, Ca, and Na in A site as a variable. These contents are determined on the basis of the average Fe^{3+} model of Leake *et al.* (1997). The residual standard errors are 0.29 for ln*D*Rb, 0.45 for ln*D*Nb, 0.23 for ln*D*Pb, 0.19 for ln*D*Sr, and 0.49 for ln*D*Zr (Humphreys *et al.*, 2019).

RESULTS

Our rock sample of Yufu Summit lava mainly contains plagioclase, amphibole as phenocryst, (Fig. 2a, b). The amphibole phenocrysts in Yufu summit lava are mostly euhedral with wide range of size (0.1–1.0 mm). The relatively coarse-grained amphiboles often contain plagioclase, pyroxene and opaque minerals, while melt inclusions are absent in all amphibole phenocrysts. The reaction rim composed of pyroxene are often observed (Fig. 2c). Some amphiboles are partially decomposed to pyroxene and opaque minerals. The plagioclases in Yufu summit lava exhibit euhedral with wide range of length (<0.1–4.0 mm). Their zonings commonly show oscillatory zoning and dusty zone composed of microscopic glass inclusions (Fig. 2a, b). Occasionally, honeycomb texture is also observed. Furthermore, coexistence of olivine and quartz is observed in the same thin section (Fig. 2a, b). The quartz phenocrysts show resorption. These petrographic features are consistent with previous studies (e.g. Hoshizumi *et al.*, 1988; Ohta *et al.*, 1990).

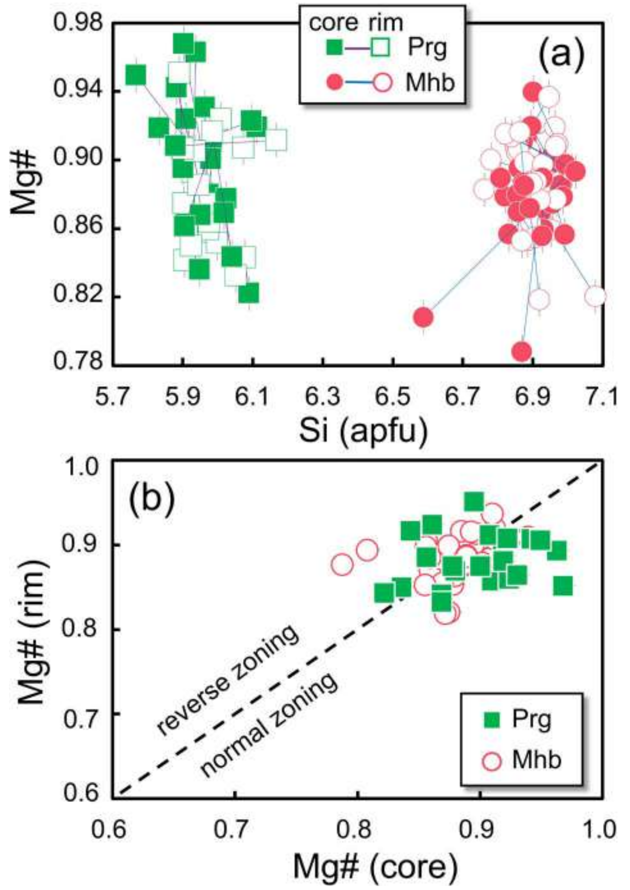

Fig. 3. Major-element compositions of amphiboles from the Yufu Summit andesite. (a) Bivariate plot of Mg# versus Si atoms per formula unit (apfu), (b) Mg# in amphibole cores and rims. Mg# values and Si contents were calculated with the sum of cations of elements (excluding Ca, Na, and K) as 13 (Leake *et al.*, 1997). Solid lines in (a) connect the cores and rims of individual grains. The gray bars for Prg and Mhb are the error bars. The bars of Si in (a) and Mg# in (b) are same size as the symbols.

The major-element compositions of core and rim in amphiboles from Yufu Summit lava are plotted on a diagram of Si atoms per formula unit (apfu) and Mg# [= $Mg/(Mg + Fe^{2+})$] in Fig. 3a and presented in Table 1. Both Si content and Mg# were calculated using the sum of cations of elements (excluding Ca, Na, and K) as 13 (Leake *et al.*, 1997). In Fig. 3a, Mg# shows a range of 0.82 to 0.97 without a gap, whereas Si shows a range of 5.7 to 7.1 apfu with a clear gap at 6.2 to 6.5 apfu, allowing low-Si and high-Si amphibole to be identified. Based on Leake's (1968) classification, low-Si and high-Si amphiboles are classified as Prg and Mhb, respectively. It is difficult to distinguish those two groups from petrographically (Fig. 2d, e). Fig. 3b show the Mg# of the amphibole cores on the

Table 1: Major-element compositions (wt %) of individual amphiboles from the Yufu Summit lava

Sample		SiO_2	TiO_2	Al_2O_3	Cr_2O_3	FeO*	MnO	MgO	CaO	Na_2O	K_2O	Total
prg-1	core	41.49	2.40	13.37	0.19	9.39	0.15	15.40	11.90	2.36	0.40	97.05
	rim	40.98	2.41	13.74	0.02	10.73	0.09	14.20	11.67	2.28	0.44	96.54
prg-2	core	41.26	2.34	13.35	0.04	9.26	0.09	15.92	11.73	2.44	0.39	96.80
	rim	41.06	2.25	14.00	0.09	9.22	0.13	15.37	12.21	2.48	0.41	97.21
prg-3	core	40.87	2.34	13.70	0.08	9.82	0.11	15.34	11.32	2.46	0.42	96.45
	rim	41.72	2.60	13.32	0.02	11.06	0.10	14.56	11.83	2.42	0.44	98.06
prg-4	core	41.11	2.60	13.55	0.03	10.17	0.07	15.31	11.87	2.29	0.40	97.41
	rim	41.19	2.33	14.02	b.d.l	10.32	0.08	14.41	11.77	2.34	0.48	96.94
prg-5	core	40.63	2.41	14.10	0.15	9.13	0.06	15.38	11.79	2.32	0.42	96.39
	rim	41.20	2.66	13.40	0.04	10.39	0.13	14.85	11.80	2.40	0.43	97.29
prg-6	core	42.46	2.36	12.58	0.12	9.32	0.09	15.61	11.54	2.38	0.35	96.82
	rim	42.31	2.43	12.65	b.d.l	10.25	0.10	15.34	11.56	2.41	0.38	97.44
prg-7	core	40.55	2.44	13.89	0.06	9.71	0.10	14.89	12.09	2.49	0.42	96.64
	rim	40.81	2.40	13.95	b.d.l	11.44	0.11	14.16	12.06	2.35	0.41	97.70
prg-8	core	42.32	2.36	12.32	0.09	9.38	0.09	15.85	11.62	2.49	0.36	96.89
	rim	40.37	2.33	13.61	0.22	9.04	0.08	15.45	12.08	2.47	0.45	96.08
prg-9	core	40.98	2.28	13.33	0.05	10.83	0.14	14.47	11.70	2.22	0.47	96.45
	rim	41.62	2.66	13.70	0.04	10.12	0.07	14.96	11.95	2.43	0.43	97.97
prg-10	core	41.37	2.22	13.69	0.05	9.65	0.07	15.15	11.75	2.49	0.39	96.83
	rim	40.54	2.65	13.44	b.d.l	10.97	0.13	14.52	11.84	2.33	0.41	96.83
prg-11	core	41.51	2.23	13.88	0.07	9.25	0.09	15.49	11.78	2.43	0.38	97.10
	rim	41.29	2.45	13.34	0.03	11.20	0.10	14.44	11.73	2.32	0.48	97.38
prg-12	core	41.42	2.23	13.50	0.04	9.03	0.11	15.23	12.02	2.47	0.36	96.41
	rim	41.23	2.24	14.00	0.07	9.53	0.12	14.98	11.93	2.57	0.44	97.10
prg-13	core	40.87	2.35	14.06	0.04	9.66	0.06	14.70	12.02	2.46	0.42	96.63
	rim	41.20	2.44	13.81	0.08	9.72	0.11	15.09	11.96	2.48	0.41	97.29
prg-14	core	40.22	2.62	13.55	0.14	9.74	0.10	14.36	11.88	2.49	0.44	95.55
	rim	40.68	2.64	13.33	b.d.l	11.45	0.15	14.23	11.79	2.44	0.39	97.08
prg-15	core	40.21	2.40	14.11	0.02	10.35	0.09	14.19	11.86	2.28	0.35	95.85
	rim	41.84	2.34	13.17	0.14	9.45	0.11	15.62	11.67	2.54	0.40	97.26
prg-16	core	41.47	2.37	12.90	0.05	10.22	0.10	14.36	11.89	2.33	0.42	96.12
	rim	41.87	2.55	12.53	b.d.l	10.94	0.15	14.58	11.74	2.38	0.44	97.19
prg-17	core	41.86	2.47	13.63	0.14	9.23	0.11	15.24	12.03	2.64	0.25	97.60
	rim	41.70	2.17	13.95	b.d.l	9.74	0.15	14.43	11.71	2.75	0.34	96.96
prg-18	core	41.62	2.43	12.75	b.d.l	11.19	0.17	14.49	11.76	2.43	0.48	97.31
	rim	41.95	2.48	13.16	0.04	10.27	0.11	15.50	11.72	2.51	0.45	98.17
prg-19	core	40.91	1.97	14.21	0.04	10.61	0.10	14.75	11.99	2.38	0.37	97.34
	rim	41.16	2.20	14.22	0.22	9.64	0.11	15.39	11.69	2.46	0.40	97.49
prg-20	core	40.34	2.45	14.58	0.05	10.17	0.15	15.37	11.94	2.53	0.42	98.00
	rim	41.22	2.33	13.91	0.04	9.48	0.08	15.36	12.02	2.44	0.43	97.30
prg-21	core	40.61	2.32	14.25	b.d.l	10.81	0.10	14.93	11.86	2.44	0.43	97.73
	rim	41.05	2.21	13.96	0.06	9.90	0.05	15.36	12.16	2.42	0.41	97.59
prg-22	core	41.09	2.43	14.26	0.03	10.08	0.12	15.15	12.11	2.31	0.42	98.00
	rim	42.69	2.01	11.70	b.d.l	11.73	0.18	14.76	11.11	2.21	0.35	96.76
mhb-1	core	48.67	1.22	6.80	0.02	12.20	0.51	15.88	10.98	1.20	0.35	97.82
	rim	49.21	1.00	6.63	0.02	12.14	0.55	15.74	10.65	1.17	0.31	97.43
mhb-2	core	48.53	1.25	6.89	b.d.l	12.12	0.49	15.66	10.86	1.20	0.36	97.35
	rim	47.88	1.05	7.05	b.d.l	12.12	0.54	15.51	10.89	1.22	0.31	96.57
mhb-3	core	47.54	1.40	7.50	b.d.l	12.11	0.48	15.09	11.06	1.29	0.46	96.96
	rim	48.54	1.20	6.79	0.02	11.92	0.51	15.91	11.04	1.23	0.35	97.51
mhb-4	core	49.14	1.18	6.56	b.d.l	11.28	0.54	16.14	11.17	1.12	0.38	97.51
	rim	48.39	1.49	7.28	0.04	12.13	0.56	15.45	10.71	1.25	0.37	97.66
mhb-5	core	48.89	1.12	6.68	b.d.l	11.90	0.59	16.12	10.87	1.16	0.31	97.66
	rim	48.92	1.10	6.48	b.d.l	11.66	0.52	15.87	10.78	1.23	0.26	96.81
mhb-6	core	47.84	1.33	7.24	b.d.l	11.63	0.57	15.36	11.00	1.28	0.37	96.62
	rim	48.45	1.24	7.21	b.d.l	12.02	0.58	15.51	10.89	1.21	0.40	97.51
mhb-7	core	48.29	1.15	6.98	b.d.l	12.21	0.61	15.60	10.95	1.14	0.32	97.24
	rim	48.82	1.09	6.60	b.d.l	11.72	0.48	15.94	10.57	1.17	0.33	96.70
mhb-8	core	48.05	1.18	7.28	0.06	11.64	0.53	15.66	10.86	1.21	0.40	96.86
	rim	48.30	1.24	6.92	b.d.l	11.93	0.50	15.93	11.15	1.21	0.34	97.53
mhb-9	core	47.90	1.40	7.41	b.d.l	12.45	0.60	15.22	10.95	1.31	0.42	97.66
	rim	47.21	1.44	7.71	b.d.l	12.31	0.50	15.21	11.15	1.17	0.42	97.13
mhb-10	core	48.51	1.22	7.36	b.d.l	12.05	0.49	15.64	11.08	1.22	0.34	97.90
	rim	47.78	1.23	7.67	b.d.l	12.64	0.58	15.29	10.83	1.39	0.41	97.83

(Continued)

Table 1: Continued

Sample		SiO_2	TiO_2	Al_2O_3	Cr_2O_3	FeO*	MnO	MgO	CaO	Na_2O	K_2O	Total
mhb-11	core	48.54	1.13	6.94	0.03	12.15	0.55	15.45	11.21	1.20	0.40	97.58
	rim	48.66	1.13	6.83	b.d.l	11.83	0.64	15.42	11.23	1.16	0.37	97.28
mhb-12	core	49.02	1.21	6.49	b.d.l	11.47	0.47	16.12	11.13	1.11	0.34	97.37
	rim	49.31	1.22	6.62	0.03	11.69	0.50	15.77	11.13	1.10	0.30	97.66
mhb-13	core	48.75	1.14	6.79	0.03	11.73	0.57	16.09	11.08	1.17	0.35	97.70
	rim	49.10	1.15	6.54	0.02	11.82	0.54	15.70	10.94	1.13	0.37	97.31
mhb-14	core	48.26	1.28	7.05	b.d.l	11.99	0.48	15.64	11.07	1.28	0.35	97.39
	rim	48.60	1.20	6.93	b.d.l	11.91	0.47	15.69	11.27	1.19	0.30	97.56
mhb-15	core	48.25	1.29	7.03	0.02	11.94	0.58	15.25	11.07	1.25	0.36	97.04
	rim	48.35	1.29	7.11	b.d.l	11.87	0.52	15.42	11.10	1.20	0.35	97.23
mhb-16	core	48.46	1.13	6.98	b.d.l	12.21	0.55	15.40	11.04	1.20	0.39	97.35
	rim	49.07	1.06	6.38	0.02	11.68	0.53	15.09	11.17	1.12	0.32	96.45
mhb-17	core	49.28	1.27	6.55	b.d.l	11.56	0.48	15.94	11.16	1.08	0.34	97.66
	rim	48.96	1.20	6.07	b.d.l	11.61	0.48	16.25	11.09	1.14	0.35	97.16
mhb-18	core	48.58	1.31	7.24	b.d.l	12.05	0.50	15.60	10.99	1.28	0.43	97.99
	rim	48.73	1.18	7.26	b.d.l	12.35	0.56	15.64	10.78	1.28	0.33	98.12
mhb-19	core	48.46	1.40	6.94	0.04	11.69	0.51	15.90	11.32	1.25	0.37	97.87
	rim	48.09	1.26	6.93	b.d.l	12.11	0.44	15.49	11.06	1.11	0.41	96.91
mhb-20	core	45.24	1.96	9.08	0.02	12.86	0.49	13.86	11.14	1.41	0.58	96.64
	rim	49.08	0.99	6.19	b.d.l	11.67	0.46	15.92	10.94	1.14	0.37	96.76
mhb-21	core	48.51	1.19	6.93	0.03	12.14	0.52	15.36	10.97	1.26	0.37	97.28
	rim	48.33	1.39	6.77	b.d.l	11.86	0.46	15.59	11.02	1.17	0.31	96.91
mhb-22	core	48.92	1.28	6.47	b.d.l	11.65	0.58	15.63	11.01	1.13	0.30	96.96
	rim	48.17	1.52	7.09	b.d.l	11.62	0.42	15.57	11.32	1.28	0.38	97.37
mhb-23	core	48.97	1.15	6.70	b.d.l	11.84	0.50	15.74	11.25	1.09	0.37	97.62
	rim	48.38	1.19	7.10	0.02	12.16	0.54	15.54	10.93	1.15	0.43	97.45
mhb-24	core	48.48	1.25	6.89	b.d.l	12.04	0.48	15.37	11.11	1.17	0.41	97.20
	rim	48.74	1.11	6.70	b.d.l	11.95	0.59	15.81	11.24	1.18	0.37	97.70
mhb-25	core	48.93	1.30	6.61	b.d.l	11.52	0.53	15.56	11.15	1.17	0.36	97.14
	rim	48.84	1.19	6.92	b.d.l	11.75	0.57	15.72	10.92	1.21	0.35	97.46
mhb-26	core	48.66	1.20	6.85	b.d.l	11.83	0.48	15.68	11.04	1.11	0.37	97.23
	rim	48.70	1.28	7.08	b.d.l	11.78	0.56	15.62	10.97	1.20	0.43	97.62
mhb-27	core	48.53	1.19	7.06	b.d.l	12.16	0.53	15.72	11.23	1.21	0.36	97.98
	rim	48.86	1.36	6.61	b.d.l	11.72	0.53	15.60	10.98	1.14	0.35	97.15
mhb-28	core	47.90	1.25	7.37	b.d.l	12.06	0.51	15.29	11.00	1.26	0.33	96.95
	rim	48.24	1.15	6.98	0.04	12.41	0.56	15.26	11.13	1.18	0.42	97.37
mhb-29	core	48.14	1.36	7.41	b.d.l	12.03	0.49	15.35	11.13	1.23	0.37	97.51
	rim	48.20	1.30	7.12	b.d.l	11.90	0.52	15.27	11.12	1.24	0.39	97.06
mhb-30	core	47.58	1.46	7.70	b.d.l	11.46	0.48	14.97	11.22	2.05	0.41	97.32
	rim	48.53	1.12	6.85	0.02	12.02	0.63	15.50	11.13	1.19	0.35	97.34
mhb-31	core	49.35	1.07	6.46	0.02	11.89	0.56	15.79	10.96	1.06	0.32	97.47
	rim	47.84	1.16	7.12	b.d.l	12.18	0.55	15.54	10.86	1.22	0.35	96.83
mhb-32	core	47.95	1.36	7.35	b.d.l	12.42	0.50	15.49	11.11	1.21	0.45	97.84
	rim	47.88	1.21	6.84	b.d.l	11.74	0.49	15.52	11.05	1.13	0.35	96.22
mhb-33	core	49.20	1.08	6.03	b.d.l	11.43	0.58	16.04	11.13	1.04	0.35	96.87
	rim	47.69	1.25	7.31	0.02	11.92	0.50	15.58	10.85	1.22	0.39	96.73
mhb-34	core	48.70	1.36	6.90	0.03	11.89	0.42	15.88	11.27	1.31	0.43	98.21
	rim	48.10	1.26	7.17	b.d.l	12.55	0.55	14.69	11.21	1.19	0.39	97.12
mhb-35	core	48.72	1.40	6.86	0.03	11.95	0.49	15.54	11.18	1.29	0.37	97.82
	rim	47.98	1.29	7.11	b.d.l	12.48	0.54	15.15	11.19	1.24	0.39	97.36

*Total Fe as FeO; b.d.l, below detection limit (<0.02 wt % for Cr_2O_3).

horizontal axis and that of the rims on the vertical axis. When the amphibole has no chemical zoning, the Mg# of core and rim show same value and are plotted on the dashed line in Fig. 3b. On the other hand, amphibole with normal and reverse zoning, in which Mg# are decrease and increase from core to rim, are plotted below and above the dashed line in Fig. 3b, respectively. The measured Mg# of Prg and Mhb are plotted on, below and above the dashed line (Fig. 3b). This observation indicates that amphiboles with and without chemical zoning are contained in Yufu Summit lava, and the differences of Mg# between core and rim are less than ≈0.1 (Fig. 3b).

DISCUSSION

Major-element compositions of amphiboles

It is considered that the Si content of amphibole varies with changing *T* and major-element compositions of the melt (Putirka, 2016; Zhang *et al.*, 2017). Based on the published data from high-*P*–*T* experiments, Zhang *et al.* (2017) suggested that amphibole with lower Si content, such as Prg, commonly crystallises in relatively high *T* (≥950°C) and mafic melt, whereas Mhb, characterised by high Si content, forms under lower *T* (<950°C) and felsic melt conditions. Such amphibole crystallisation conditions with different *T* and major-element compositions of melt suggest that

Prg and Mhb are unlikely to coexist in equilibrium. Therefore, it can be considered that Prg and Mhb in the Yufu Summit lava crystallised in relatively high-*T* and mafic magma, and low-*T* and felsic magma, respectively. Furthermore, the coexistence of such disequilibrium amphiboles cannot be explained without considering the mixing of the two different magmas. Therefore, Prg and Mhb in the Yufu Summit lava are thought to retain information on the *P*–*T* conditions and major element compositions of the melt from which they crystallised, before magma mixing occurred. On the other hand, in the plot of Mg# for core and rim in amphiboles from Yufu Summit lava (Fig. 3b), the differences of Mg# between core and rim are ≈0.1 in maximum. Thus, to clarify the effect of chemical zoning in amphiboles on the estimating the *P*–*T* conditions and major-element compositions of equilibrated melt, we estimated these values for each core and rim, and compared them as below described.

P–*T* conditions of amphibole crystallisation

Many geothermobarometers have been proposed based on equilibria between amphibole, and melt and plagioclase (e.g. Blundy & Holland, 1990, 1992; Holland & Blundy, 1994; Molina *et al.,* 2015). In the case of magma formed by magma mixing, it is difficult to use these geothermometers because it is unclear whether amphibole coexisted in equilibrium with melt and plagioclase. The *P* of amphibole crystallisation can be estimated from the Al content of amphibole (e.g. Hammarstrom & Zen, 1986; Johnson & Rutherford, 1989; Schmidt, 1992; Anderson & Smith, 1995). However, geobarometers based on the Al content of amphibole can only be applied under very limited conditions, such as granitic systems under near-solidus conditions and in equilibrium with multi-phase assemblages, for which $T < 800$°C and amphibole Fe/(Fe + Mg) < 0.65 (e.g. Hammarstrom & Zen, 1986; Anderson & Smith, 1995). Furthermore, Ridolfi *et al.* (2008) pointed out that geobarometers based on the Al content in amphibole have impractically large errors. In this study, to estimate the *P*–*T* conditions of amphibole crystallisation for individual crystals, we incorporated the major-element compositions of Prg and Mhb into the geothermometer of Putirka (2016), and geobarometers of Ridolfi & Renzulli (2012) and Ridolfi (2021). The estimated *P*–*T* conditions of core and rim for Prg and Mhb are presented in Table 2 and Fig. 4. The estimated crystallisation *T* is 932°C to 1016°C for Prg, and 773°C to 846°C for Mhb (Fig. 4; Table 2). The estimated *P* conditions for Prg and Mhb are 356 to 600 MPa and 73 to 222 MPa using the geobarometer of Ridolfi & Renzulli (2012), and 364 to 941 MPa and 117 to 212 MPa using the geobarometer of Ridolfi (2021) (Fig. 4; Table 2). Figure 5 shows the relationship between Si contents and estimated *T* for core and rim of amphibole. The estimated *T* decrease with increasing Si contents of amphiboles. This observation is consistent with previous studies (e.g. Putirka, 2016; Zhang *et al.,* 2017). It can be considered that these differences in conditions for the two amphibole types suggests that two magma reservoirs with different *P*–*T* conditions existed beneath Yufu Volcano. For an assumed crustal density of 2700 kg/m^3 (Gill, 1981), the estimated *P* conditions from the geobarometer of Ridolfi & Renzulli (2012) are equivalent to depth ranges of 13 to 23 km for Prg and 3 to 8 km for Mhb. In estimated results of the geobarometer of Ridolfi (2021), the crystallisation depth of Prg and Mhb are 14 to 36 km and 4 to 8 km, respectively. Two seismic observations, which are thought to be related to the existence of magma, have been reported at difference depth ranges beneath Yufu Volcano (Ohkura *et al.,* 2002; Nagasaki *et al.,* 2017). One is deep low-frequency earthquakes with a depth of 17 to 30 km, which is interpreted to be related to magma activity (Nagasaki *et al.,* 2017). Comparing the crystallisation depth ranges of Prg obtained from the geobarometers of Ridolfi & Renzulli (2012) and Ridolfi (2021), the latter is wider. However, most of crystallisation depth for Prg obtained from the geobarometer of Ridolfi (2021) is concentrated 16 to 21 km (411–549 MPa; Fig. 4), which is consistent with that of Ridolfi & Renzulli (2012). This depth range overlaps the upper part of the occurrence area of deep low-frequency earthquakes. This observation could be suggested the possibility that the magma ascending from a depth of ≈30 km stagnated at a depth of 13 to 23 km, and then Prg crystallised. Another is an aseismic zone with a depth of 3 to 10 km in the region of tectonic earthquakes occurring <12.5 km, which is explained by the possibility that the high *T* body exist in these area (Ohkura *et al.,* 2002). The occurrence depth of the aseismic zone overlaps the crystallisation depth of Mhb in both the geobarometers of Ridolfi & Renzulli (2012) and Ridolfi (2021). This coincidence may be interpreted as supporting evidence that the depth of the magma reservoir in which the Mhb crystallised is 3 to 8 km. Therefore, it can be suggested that the magma reservoirs in which Prg and Mhb crystallised existed at a depth of 13 to 23 km and *T* of 940°C to 1020°C, and a depth of 3 to 8 km and *T* of 780°C to 850°C, respectively. Similar observations have been reported by Okada *et al.* (2018) for amphiboles from the Imorigashiro lava, which was erupted during the early-stage of volcanic activity of Yufu Volcano (Ohta *et al.,* 1990). They divided Imorigashiro lava amphiboles into two groups with Si amounts of 5.9 to 6.3 and 6.8 to 6.9 apfu, and estimated their crystallisation depth ranges and *T* of 14 to 25 km (356–654 MPa) and 940°C to 1000°C, and 5 to 7 km (131–188 Mpa) and 800°C to 840°C, respectively. Our results for the late-stage Yufu Summit lava are indistinguishable from those of Okada *et al.* (2018) for the early-stage Imorigashiro lava, suggesting there may be no significant changes in the structure of the magma plumbing system over the period between the eruption of the two lavas.

To evaluate the influence of chemical zoning on the estimation on the *P*–*T* conditions, we compared the *T* and *P* estimated from the core and rim compositions, respectively (Fig. 6). In Fig. 6a, *T* estimated from the core and rim compositions are plotted on the horizontal and vertical axes, respectively. Both Prg and Mhb are plotted around a solid straight line where the estimated *T* from the cores and rims are same value, and deviations from a solid straight line are mostly within the error range of estimate. Similar trends are observed in crystallisation *P* (Fig. 6b, c). From these observations, it may suggest that chemical zoning does not have a significant influence on the estimation of the *P*–*T* conditions under which amphibole crystallised.

Major-element composition of melt in equilibrium with amphibole

The major-element compositions of melt in equilibrium with Prg and Mhb are estimated from the major-element composition of Prg and Mhb using equations of Zhang *et al.* (2017) and listed in Table 2. Hereafter, we term melts in equilibrium with Prg and Mhb as 'melt-Prg' and 'melt-Mhb', respectively. The major-element oxides of melt-Prg and melt-Mhb versus SiO_2 contents are plotted in Fig. 7. The trends of melt-Prg and melt-Mhb are similar to the general compositional trends of magmas from basalt to rhyolite, such as decreasing TiO_2, Al_2O_3, FeO, MgO, CaO, and increasing K_2O with increasing SiO_2 contents. These trends can be explained by fractional crystallisation from basaltic magma to rhyolitic magma. However, the estimated SiO_2 content for melt-Prg and melt-Mhb show obvious compositional gap between the two amphibole types at 62.9 to 72.2 wt %, which greatly exceeds

Table 2: Estimated crystallisation *P–T* conditions and major-element compositions of melt in equilibrium with amphibole

Sample		T (°C)	P1 (MPa)	P2 (MPa)	SiO_2 (wt %)	TiO_2 (wt %)	Al_2O_3 (wt %)	FeO* (wt %)	MgO (wt %)	CaO (wt %)	K_2O (wt %)
prg-1	core	992	517	526	56.07	1.07	18.30	6.35	3.82	7.47	1.40
	rim	980	500	491	58.54	0.93	18.31	6.04	3.19	7.19	1.14
prg-2	core	997	491	499	55.70	1.14	18.67	7.35	4.63	7.92	0.85
	rim	1004	539	548	55.22	1.05	18.82	6.80	4.69	8.45	1.04
prg-3	core	996	541	792	54.75	1.21	18.82	8.28	4.54	8.09	0.86
	rim	980	449	459	58.69	0.90	18.08	5.96	2.88	6.45	1.40
prg-4	core	993	490	490	56.67	1.13	18.45	7.10	4.23	7.47	1.01
	rim	985	516	526	57.95	0.95	18.47	6.11	3.45	7.70	1.03
prg-5	core	1005	578	735	54.33	1.29	18.83	7.75	5.22	8.85	0.89
	rim	991	484	494	57.08	1.04	18.27	6.56	3.50	6.98	1.33
prg-6	core	975	433	441	59.07	0.93	17.88	5.27	2.81	6.59	1.31
	rim	973	412	420	59.56	0.88	17.95	5.58	2.76	6.30	1.23
prg-7	core	1005	524	534	55.49	1.05	18.75	6.93	4.41	8.06	1.13
	rim	985	496	482	57.85	0.87	18.52	6.53	3.52	7.11	1.16
prg-8	core	979	408	635	58.53	0.92	17.95	5.56	2.95	6.42	1.35
	rim	1010	542	780	53.46	1.16	18.72	7.50	5.08	8.31	1.33
prg-9	core	973	483	490	58.24	0.89	18.15	6.09	3.19	6.82	1.32
	rim	994	487	497	57.34	1.05	18.33	6.29	3.54	7.32	1.22
prg-10	core	991	500	757	56.97	0.98	18.65	6.49	3.84	7.85	0.92
	rim	990	483	489	57.14	1.01	18.36	6.90	3.68	6.90	1.26
prg-11	core	994	529	538	56.30	1.08	18.74	6.77	4.31	8.33	0.81
	rim	976	463	471	58.37	0.89	18.10	6.19	3.02	6.56	1.38
prg-12	core	993	487	720	57.66	0.93	18.52	5.66	3.71	7.83	1.04
	rim	999	532	872	55.82	1.00	18.76	6.64	4.02	8.19	1.08
prg-13	core	999	525	534	56.69	1.00	18.70	6.33	4.01	8.18	1.02
	rim	999	518	527	56.03	1.06	18.61	6.73	4.06	7.84	1.14
prg-14	core	1004	522	-	55.66	1.06	18.43	6.49	3.72	7.50	1.54
	rim	987	466	474	57.67	0.91	18.32	6.72	3.22	6.48	1.39
prg-15	core	993	540	-	57.45	0.99	18.71	6.53	4.00	7.97	0.90
	rim	991	483	771	56.25	1.03	18.38	6.58	3.64	7.31	1.25
prg-16	core	974	431	441	60.18	0.78	17.83	4.72	2.51	6.37	1.55
	rim	970	401	411	60.12	0.79	17.66	5.12	2.35	5.75	1.68
prg-17	core	1000	504	791	56.98	0.98	18.58	5.93	3.56	7.62	1.19
	rim	992	516	-	57.74	0.83	18.75	5.73	3.03	7.73	1.08
prg-18	core	972	418	428	59.27	0.78	17.86	5.53	2.53	5.93	1.65
	rim	987	456	680	56.91	1.01	18.29	6.76	3.50	6.89	1.24
prg-19	core	986	534	542	56.77	0.88	18.92	6.96	4.26	8.09	0.78
	rim	999	594	941	53.79	1.19	18.93	8.14	4.87	8.61	0.99
prg-20	core	1016	600	886	52.26	1.31	19.34	9.89	6.25	9.03	0.76
	rim	999	517	526	56.04	1.07	18.73	6.84	4.46	8.23	0.91
prg-21	core	998	540	549	55.07	1.08	19.00	8.37	4.86	8.14	0.79
	rim	997	511	520	55.86	1.01	18.81	7.11	4.70	8.17	0.88
prg-22	core	998	545	530	55.89	1.12	18.76	7.23	4.70	8.27	0.89
	rim	932	356	364	62.92	0.62	17.34	4.65	1.77	4.95	3.10
mhb-1	core	792	110	132	77.06	0.21	13.43	1.04	0.28	1.98	3.06
	rim	777	108	-	77.91	0.19	13.22	0.92	0.22	1.93	3.06
mhb-2	core	791	111	-	77.31	0.21	13.41	1.01	0.27	2.01	2.96
	rim	793	125	-	77.00	0.20	13.70	1.06	0.29	2.08	3.23
mhb-3	core	808	136	151	75.88	0.23	13.65	1.11	0.30	2.17	3.13
	rim	795	110	131	76.89	0.21	13.47	1.02	0.28	2.01	3.21
mhb-4	core	789	100	156	77.79	0.20	13.16	0.85	0.26	1.98	3.16
	rim	802	145	-	75.94	0.25	13.55	1.13	0.28	2.10	3.03
mhb-5	core	788	118	-	76.97	0.21	13.40	1.02	0.28	2.01	3.03
	rim	785	96	-	78.18	0.19	13.31	0.89	0.24	1.93	3.17
mhb-6	core	805	136	148	76.29	0.22	13.63	1.03	0.29	2.14	3.14
	rim	795	135	-	76.54	0.22	13.51	1.04	0.28	2.09	3.10
mhb-7	core	790	129	-	77.12	0.20	13.50	1.03	0.28	2.03	2.89
	rim	783	102	-	77.58	0.20	13.29	0.97	0.25	2.01	3.07
mhb-8	core	800	144	153	75.75	0.23	13.66	1.10	0.31	2.21	3.03
	rim	799	112	133	76.88	0.21	13.57	1.05	0.31	2.07	3.26
mhb-9	core	805	146	153	75.64	0.23	13.70	1.17	0.30	2.10	3.04
	rim	810	150	159	75.76	0.25	13.83	1.22	0.36	2.26	2.93
mhb-10	core	798	128	146	77.01	0.21	13.69	1.05	0.30	2.16	3.04
	rim	807	157	161	74.89	0.23	14.02	1.32	0.33	2.21	3.34

(Continued)

Table 2: Continued

Sample		T (°C)	P1 (MPa)	P2 (MPa)	SiO_2 (wt %)	TiO_2 (wt %)	Al_2O_3 (wt %)	FeO* (wt %)	MgO (wt %)	CaO (wt %)	K_2O (wt %)
mhb-11	core	790	114	134	77.43	0.19	13.33	0.92	0.25	1.97	3.41
	rim	788	118	134	77.85	0.18	13.22	0.84	0.24	1.94	3.12
mhb-12	core	788	90	122	78.19	0.20	13.16	0.86	0.26	1.95	3.20
	rim	783	95	126	78.86	0.19	13.08	0.80	0.23	1.91	3.15
mhb-13	core	793	120	135	76.73	0.21	13.44	1.00	0.29	2.04	3.28
	rim	781	99	-	78.26	0.19	13.06	0.84	0.22	1.89	3.07
mhb-14	core	800	113	136	76.90	0.21	13.59	1.03	0.29	2.07	3.06
	rim	793	102	130	78.13	0.19	13.44	0.91	0.27	2.02	3.34
mhb-15	core	796	125	140	77.14	0.20	13.41	0.93	0.25	2.00	3.17
	rim	796	121	140	77.41	0.21	13.44	0.94	0.27	2.05	3.23
mhb-16	core	789	116	136	77.47	0.19	13.39	0.95	0.25	1.99	3.52
	rim	774	79	117	80.28	0.15	12.83	0.63	0.17	1.75	3.18
mhb-17	core	785	89	-	78.77	0.19	13.03	0.81	0.23	1.92	3.25
	rim	785	76	113	78.05	0.19	12.99	0.87	0.24	1.84	3.15
mhb-18	core	800	125	143	76.37	0.22	13.55	1.06	0.28	2.10	2.96
	rim	794	136	-	76.46	0.21	13.68	1.12	0.28	2.10	3.26
mhb-19	core	805	116	134	76.47	0.22	13.46	1.01	0.30	2.05	3.13
	rim	792	104	132	77.69	0.21	13.34	0.97	0.28	2.01	3.27
mhb-20	core	846	222	212	72.19	0.33	14.42	1.68	0.46	2.62	3.19
	rim	776	73	-	78.79	0.17	13.00	0.80	0.22	1.84	3.27
mhb-21	core	791	114	135	77.38	0.19	13.39	0.94	0.24	1.96	3.11
	rim	795	101	129	77.99	0.21	13.32	0.93	0.26	1.97	3.31
mhb-22	core	785	99	125	78.62	0.19	13.07	0.81	0.22	1.86	3.20
	rim	808	105	133	77.07	0.22	13.44	0.96	0.29	2.08	3.22
mhb-23	core	785	95	125	78.57	0.18	13.14	0.83	0.24	1.94	3.18
	rim	792	128	-	76.66	0.21	13.42	1.04	0.28	2.06	3.27
mhb-24	core	790	103	131	77.98	0.19	13.24	0.89	0.24	1.96	3.31
	rim	789	109	129	77.44	0.19	13.31	0.91	0.26	1.95	3.39
mhb-25	core	789	97	126	78.43	0.19	13.07	0.79	0.22	1.90	3.13
	rim	791	120	138	77.29	0.20	13.40	0.94	0.26	2.03	3.09
mhb-26	core	788	104	132	78.00	0.20	13.28	0.91	0.26	2.01	3.22
	rim	795	125	142	76.83	0.22	13.40	0.97	0.27	2.06	3.11
mhb-27	core	795	116	136	77.19	0.20	13.53	1.00	0.29	2.05	3.29
	rim	788	100	128	78.30	0.20	13.09	0.84	0.23	1.90	3.00
mhb-28	core	801	132	148	76.88	0.21	13.73	1.05	0.29	2.15	3.39
	rim	790	119	136	77.21	0.19	13.33	0.96	0.25	1.95	3.07
mhb-29	core	803	129	147	76.90	0.22	13.62	1.03	0.29	2.14	3.27
	rim	798	118	139	77.27	0.20	13.43	0.93	0.26	2.04	3.44
mhb-30	core	840	132	147	73.76	0.21	14.35	1.15	0.30	2.23	3.34
	rim	789	122	136	77.34	0.19	13.35	0.92	0.25	1.96	3.21
mhb-31	core	775	97	-	78.78	0.18	12.97	0.81	0.21	1.87	3.01
	rim	796	132	145	76.40	0.22	13.71	1.13	0.31	2.10	3.15
mhb-32	core	803	132	146	76.02	0.23	13.63	1.16	0.32	2.12	3.12
	rim	793	109	133	77.65	0.20	13.39	0.94	0.28	2.03	3.37
mhb-33	core	776	80	-	78.98	0.17	12.81	0.75	0.21	1.80	2.97
	rim	803	138	151	75.85	0.24	13.76	1.17	0.33	2.21	3.27
mhb-34	core	803	100	128	76.59	0.21	13.39	1.00	0.28	2.02	3.43
	rim	790	116	137	78.31	0.18	13.29	0.86	0.23	1.92	3.35
mhb-35	core	798	104	130	77.39	0.20	13.31	0.92	0.25	1.95	3.31
	rim	797	118	136	77.22	0.19	13.46	0.99	0.27	1.98	1.24

*Total Fe as FeO. P1 and P2 are crystallisation *P* of amphibole estimated by the geobarometers of Ridolfi & Renzulli (2012) and Ridolfi (2021), respectively. Hyphens mean failure to pass the composition filter of amphibole for applying the geobarometer of Ridolfi (2021).

the error in estimated SiO_2 content (±3.29 wt %; Zhang *et al.*, 2017). From this observation, it can be pointed out that the trends in the major-element compositions of melt-Prg and melt-Mhb indicate independent crystallisation trends of the two magmas, each of which has a different origin. A more detailed view of the trend on Fig. 7 for melt-Prg and melt-Mhb, they can be considered to be more linear than curvilinear. If this is a case, the trend of melt-Prg and melt-Mhb can be explained by two-component mixing. Furthermore, there must be at least three-component mixing, since the melt-Prg and melt-Mhb trends other than Al_2O_3 and K_2O in Fig. 7 are not distributed on single straight lines. Trends in the chemical composition of melt-Prg and melt-Mhb are discussed further in 'Trace-element composition of melt in equilibrium with amphibole' section.

The estimated SiO_2 contents of melt-Prg and melt-Mhb are basaltic–dacitic (SiO_2 = 52.3–62.9 wt %) and rhyolitic (SiO_2 = 72.2–80.3 wt %), respectively (Fig. 7). For the other estimated major-element compositions (Fig. 7), melt-Prg has higher TiO_2, Al_2O_3, FeO, MgO, and CaO and lower K_2O contents (0.62–1.31, 17.7–19.3, 4.65–9.89, 1.77–6.25, 4.95–9.02, and 0.78–1.68 wt %, respectively)

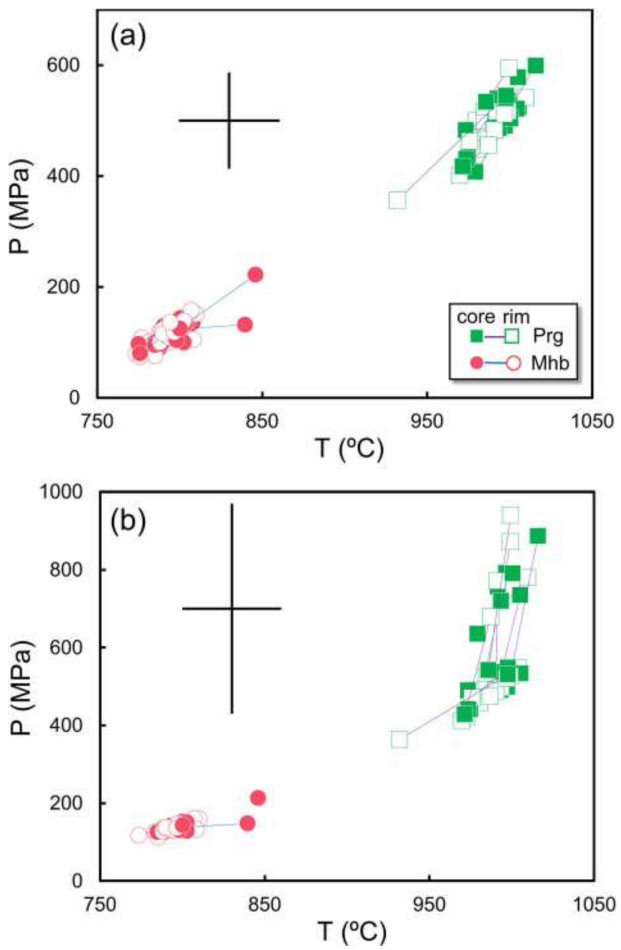

Fig. 4. Crystallisation *P*–*T* conditions of amphiboles. The crystallisation *P* in (a) and (b) were estimated using geobarometers of Ridolfi & Renzulli (2012) and Ridolfi (2021), respectively. The solid lines connect the cores and rims of individual grains. Cross-bars represent the error bars.

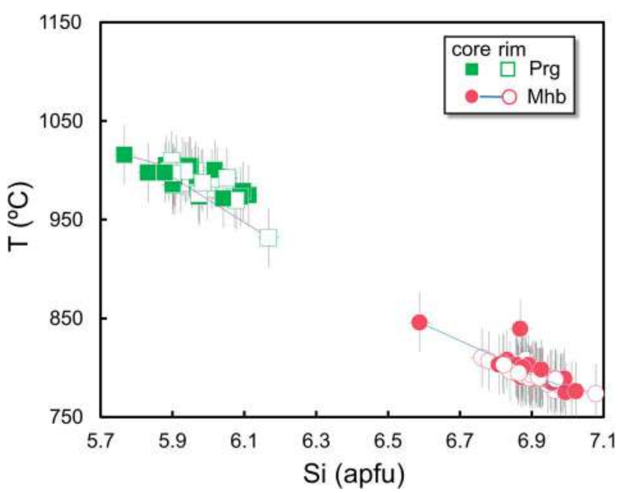

Fig. 5. The relationship between Si content and crystallisation *T* condition for amphiboles. The solid lines connect the cores and rims of individual grains. The gray bars for Prg and Mhb are the error bars.

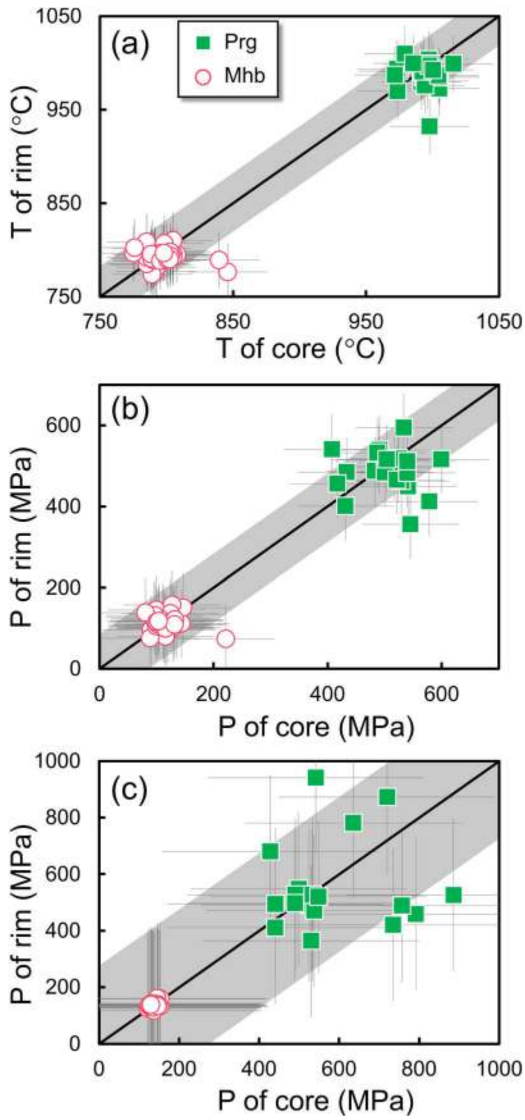

Fig. 6. Comparisons between core and rim for estimated *T* (a) and *P* (b and c). The crystallisation *P* in (b) and (c) were estimated using geobarometers of Ridolfi & Renzulli (2012) and Ridolfi (2021), respectively. The solid lines represent 1:1 relationship. The estimation errors are shown as grey zones for solid lines, and as gray bars for individual amphiboles.

compared with melt-Mhb (0.15–0.33, 12.8–14.4, 0.63–1.68, 0.17–0.16, 1.75–2.62, and 2.89–3.52 wt %, respectively). These results suggest that Prg and Mhb in the Yufu Summit lava crystallised from two different magmas with distinct chemical compositions as well as different *P*–*T* conditions, and indicate that Prg and Mhb in the Yufu Summit lava crystallised from mafic and felsic magmas, respectively, as proposed by Ohta *et al.* (1990) and Ohta & Aoki (1991) based on the petrological and geochemical features of volcanic products from Yufu Volcano. Kent (2014) showed that two types of amphiboles, crystallised from deep and hot mafic magma and shallow and cool felsic magma, respectively, are observed from intermediate lavas in convergent margins, such as Mont Pelée, Soufriére Hills, Unzen, and Mount Hood. From this observation, they pointed out that such widespread presence of two groups of amphibole emphasises the global importance of magma mixing in the genesis of andesitic magma, and is important evidence of magma mixing. The coexistence of Prg and Mhb in Yufu Summit lava, therefore, can be explained by the mixing of these two magmas. This argument is supported by the disequilibrium textures, such as resorbed quartz, coexistence of olivine and quartz, and oscillatory zoning, dusty zone and honey-comb texture in plagioclase phenocrysts, which are

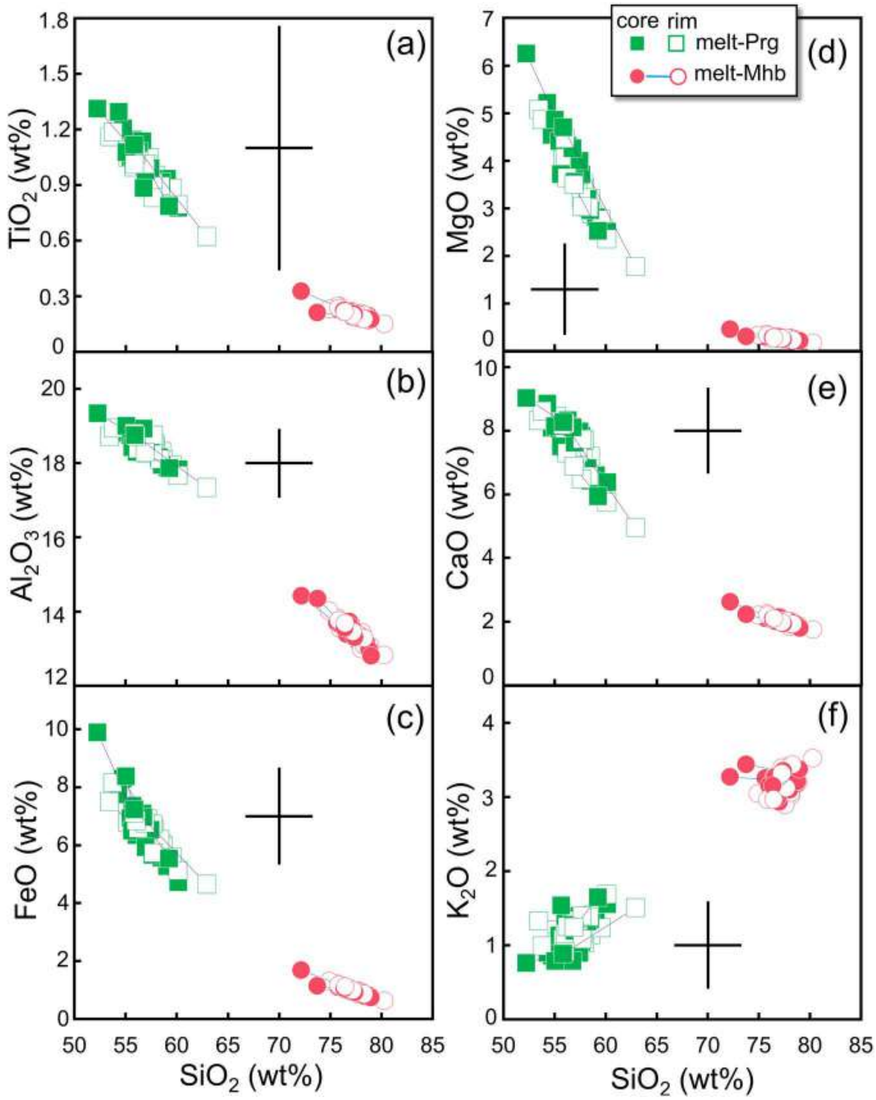

Fig. 7. Bivariate plots of major-element oxide contents versus SiO_2 content for melts in equilibrium with amphiboles. (a) TiO_2; (b) Al_2O_3; (c) FeO; (d) MgO; (e) CaO; (f) K_2O. Solid lines connect the cores and rims of individual grains. Cross-bars denote the error range.

considered as a result of magma mixing (e.g. Eichelberger, 1978; Sakuyama, 1979, 1981; Tsuchiyama, 1986; Kawamoto, 1992; Singer *et al.*, 1995) (Fig. 2a, b).

The major-element compositions of melt-Prg and melt-Mhb from the core and rim are plotted in Fig. 8 to evaluate the effects of chemical zoning in amphiboles to the estimation of the major-element compositions of melts in equilibrium with amphibole. Figure 8a plots the SiO_2 content of melt in equilibrium with amphibole estimated from the core and rim compositions on the horizontal and vertical axes, respectively. Both melt-Prg and melt-Mhb are mostly plotted around a solid straight line, where the estimated SiO_2 from the cores and rims are same value, within error range of estimate. Similar trends are observed for other elements (Fig. 8b-g). These observations suggest that inside of the grains of each amphibole measured in this study are chemically homogeneous within estimating error.

Trace-element composition of melt in equilibrium with amphibole

It has been suggested that the *Kd*s for trace-elements between amphibole and melt vary widely with *P*–*T* conditions, melt composition, and amphibole crystal structure (e.g. Tiepolo *et al.*, 2007). In the case of this study, as discussed above, the two groups of amphiboles in the Yufu Summit lava crystallised under different *T* and *P* conditions and from melts with distinct compositions (Figs. 4 and 7). Therefore, the use of published *Kd*s between amphibole and melt that were determined under conditions of fixed *T*, *P*, and melt composition results in large uncertainty. This makes it difficult to determine the values of *Kd*s, which are important for accurately estimating the trace-element compositions of melt in equilibrium with amphibole. To overcome this problem, *Kd*s was estimated independently using the method of Shimizu *et al.* (2017) for REEs and Y, and equations of Humphreys *et al.* (2019) for Rb, Nb, Pb, Sr and Zr from the major-element compositions of amphibole and estimated *T* for each grain in the previous section. The calculated *Kd*s and trace-element compositions of melt-Prg and melt-Mhb are listed in Table 3. The *Kd*s of REEs excluding Pr, Tb, Er, and Tm can be calculated by both Shimizu *et al.* (2017) and Humphreys *et al.* (2019). For comparison, these *Kd*s calculated using Humphreys *et al.* (2019) are plotted on Supplementary Figure against those of Shimizu *et al.* (2017). The values of *Kd*s calculated by Humphreys

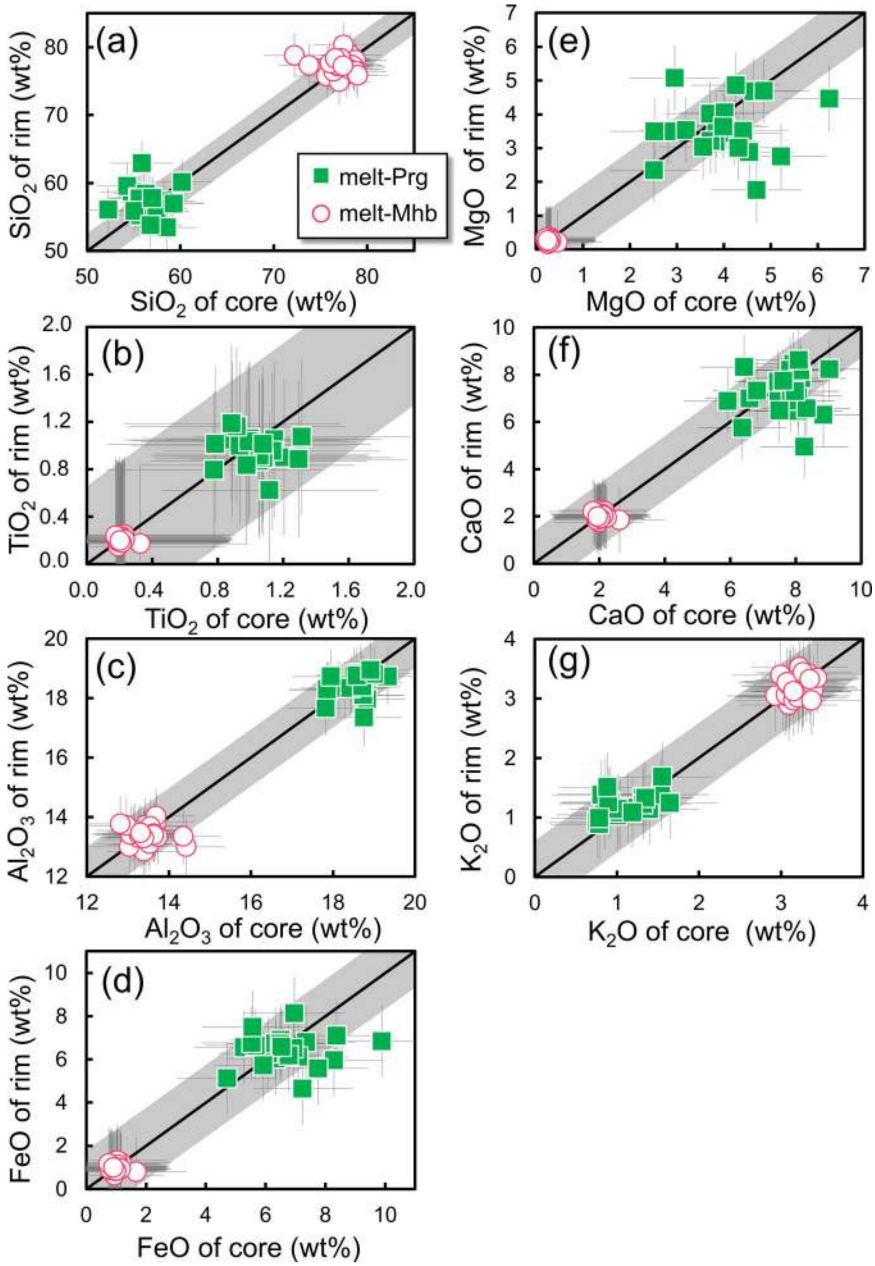

Fig. 8. Comparisons between core and rim for major-element compositions of melt in equilibrium with amphiboles. The solid lines represent 1:1 relationship. The estimation errors are shown as grey zones for solid lines, and as gray bars for individual amphiboles.

et al. (2019) are within error ranges of Shimizu *et al.* (2017), except for Ho and Lu in Mhb. From these observations, it can be considered permissible to assume that either method makes no significant difference, with the exception for Ho and Lu in melt-Mhb, in the estimation of trace-element compositions of melts in equilibrium with amphiboles in Yufu Summit lava. We applied the calculated *Kd*s to the trace-element composition of individual amphiboles in the Yufu Summit lava (Table 4) to determine the trace-element compositions of melt-Prg and melt-Mhb. The estimated results of trace-element compositions of melt-Prg and melt-Mhb are listed in Table 5, and shown in Fig. 9 as the primitive-mantle-normalised trace-element patterns (PM patterns) diagram. For normalisation, the values of primitive mantle of Sun & McDonough (1989) are used. The compositions of melt-Prg and melt-Mhb are similar to those of typical island-arc magmas, characterised by enrichments in large ion lithophile elements (LILEs; e.g. Rb, Pb, and Sr), and depletions in Nb and Zr (e.g. Wood *et al.*, 1979; Perfit *et al.*, 1980) (Fig. 9). However, the following differences are observed between melt-Prg and melt-Mhb in the PM patterns diagram (Fig. 9): 1) the PM patterns of melt-Prg and melt-Mhb show positive and negative Sr spikes, respectively; 2) melt-Prg is more depleted in LILEs (except for Sr) than melt-Mhb; 3) melt-Prg has higher contents of middle REEs, and lower Yb and Lu than melt-Mhb. These features can be observed more clearly in the relationship between Sr/Y ratios and Y (Fig. 10). We also show the fields of adakite and common island-arc andesite, dacite and rhyolite (ADR), as defined by Defant & Drummond (1990), in Fig. 10. Although Y contents of melt-Prg and melt-Mhb are similar (≈8–9 ppm) to each other, the Sr/Y values of melt-Prg are higher (≈100–200) and plot within the adakite field (Defant & Drummond, 1990), whereas those of melt-Mhb are lower (≈20–40) and plot outside the fields of adakite and common island-arc ADR (Defant & Drummond, 1990) (Fig. 10). These differences suggest that Prg and Mhb were crystallised from different magmas in terms of trace-element compositions as well as *T* and *P* conditions and major-element compositions.

To confirm whether the estimated trace-element compositions of melts in equilibrium with amphiboles in the Yufu Summit lava are realistic, we compared the PM patterns and relationships between Sr/Y and Y of melt-Prg and melt-Mhb with those of dacite and rhyolite from the Himeshima volcanic group (HVG; Fig. 1b) (Shibata *et al.*, 2014) and volcanic glass from the Kuju volcanic group (KVG; Fig. 1b) (Albert et al., 2019) from the Quaternary volcanoes located near Yufu Volcano. The PM pattern of dacite from the HVG (Fig. 9) is similar to that of melt-Prg except for Rb and Zr. In addition, the Sr/Y ratios and Y contents of dacite from the HVG plot close to those of melt-Prg and within the adakite field (Fig. 10). The PM patterns of rhyolite from the HVG (Shibata *et al.*, 2014) and volcanic glass from the KVG (Fig. 1b) (Albert et al., 2019) are also shown in Fig. 9. The patterns for melt-Mhb and rhyolite from the HVG are similar except for La, Ce, and Sr, and those for melt-Mhb and volcanic glass from the KVG are very similar except for Zr. Furthermore, as in the case for melt-Mhb, rhyolites from the HVG (Shibata *et al.*, 2014) and volcanic glass from the KVG (Albert et al., 2019) have low Sr/Y ratios and Y contents that plot outside of both the adakite and common island-arc ADR fields (Defant & Drummond, 1990) (Fig. 10). These observations, despite small differences, would allow us to believe that the PM patterns and relationship between Sr/Y and Y of melt-Prg and melt-Mhb, determined from the trace-element compositions of Prg and Mhb using the estimated *Kd*s, were not unrealistic. This may indicate that the estimated *Kd*s uncertainty can be assumed to be within an acceptable range for discussing the trace-element compositions of the melts in equilibrium with amphiboles from Yufu Summit lava.

In a study of Quaternary magmas from northern Kyushu, Shibata *et al.* (2014) reported that $^{87}Sr/^{86}Sr$ decreases with increasing SiO_2 and that dacites from the HVG show the lowest values ($^{87}Sr/^{86}Sr \approx 0.7037$) with highest Sr/Y ratios (Sr/Y ≈ 100). From those geochemical features, those authors inferred that dacitic magma from the HVG was derived from adakitic magma that originated by slab melting of subducted Philippine Sea Plate (PSP). Moreover, Sugimoto *et al.* (2006) reported that some andesites from Yufu Volcano have adakitic features (Sr/Y = 42 and $^{87}Sr/^{86}Sr = 0.7039$). The whole-rock trace-element and Sr–Nd–Pb isotopic compositions of adakitic rocks from Yufu Volcano are thought to have been derived from the partial melting of subducting PSP (Sugimoto *et al.*, 2006). Young PSP (26–15 Ma; Mahony *et al.*, 2011) is subducted underneath the Southwest Japan arc, including Yufu Volcano and the HVG (Fig. 1b). This is a tectonic setting that fully satisfies the conditions under which slab melting occurs (Defant & Drummond, 1990). In fact, adakitic lavas, which are ascribed to a slab-melt origin, have also been observed at Daisen, Sambe, Aonoyama, Futagoyama, and Kuju Volcanoes in the Southwest Japan Arc (Fig. 1b) (e.g. Morris, 1995; Kimura *et al.*, 2005, 2014; Shibata *et al.*, 2014). Therefore, Prg may have crystallised from adakitic magma derived from the melting of subducted PSP.

Rhyolite from the HVG and volcanic glass from the KVG are volcanic products from explosive eruptions (Itoh, 1989;Kawanabe *et al.*, 2015 ; Albert et al., 2019). In particular, the latter is derived from large-scale Plinian eruptions (Kawanabe *et al.*, 2015; Albert *et al.*, 2019). It is widely argued that the felsic magma that can generate such eruptions originates from the partial melting of crustal material (e.g. Sisson *et al.*, 2005; Kimura & Nagahashi, 2007; Bindeman *et al.*, 2010; Folkes *et al.*, 2013; Kimura *et al.*, 2015) on the basis of the following lines of evidence: 1) the major-element compositions of volcanic products from large eruptions are similar to those of melts obtained from melting experiments of sedimentary, granitic, and amphibolitic rocks (Sisson *et al.*, 2005; Kimura & Nagahashi, 2007; Kimura *et al.*, 2015); 2) the major- and trace-element compositions of volcanic glass from large-scale eruptions can be reproduced by model calculations of partial melting of granites, sediments, and amphibolites (Kimura *et al.*, 2015); and 3) the O, Sr, and Nd isotopic compositions of volcanic products from large eruptions are similar to those of crustal rocks (Kimura & Nagahashi, 2007; Bindeman *et al.*, 2010; Folkes *et al.*, 2013). Considering the above, we infer that the felsic magmas that produced the HVG rhyolite and KVG volcanic glass originated from the partial melting of crustal material, although the origins of these magmas are currently unknown. Given this inference, melt-Mhb may also have been derived from crustal melting.

Chemical variations of melts in equilibrium with amphiboles

The process making the variations in major-element compositions of melt-Prg and melt-Mhb are discussed in previous section, but it is still ambiguous. In this section, therefore, we discuss the process using melt-Prg and melt-Mhb major-element compositions as well as trace-element compositions. In Fig. 11, the Y/Rb and Dy/Rb ratios against Sr/Rb ratios are plotted. For both melt-Prg and melt-Mhb, Y/Rb and Dy/Rb ratios decrease with decreasing of Sr/Rb ratios. The trend of melt-Prg shows higher Sr/Rb ratios and gentler slope compared to melt-Mhb. In previous section, four scenarios that could explain the variation in major-element compositions of melt-Prg and melt-Mhb was presented as follows: 1) crystal fractionation from basaltic to rhyolitic melt forming continuous trend from melt-Prg and melt-Mhb, 2) two different crystallisation processes formed the melt-Prg and melt-Mhb trends independently, 3) three-components mixing including one component common to melt-Prg and melt-Mhb, 4) using four-components, melt-Prg and melt-Mhb independently formed a trend in two-components mixing. If 1) and 3) are the case, melt-Prg and melt-Mhb should show a trend that can be explained by a continuous trend such as Fig. 7, although there is a compositional gap, in Fig. 11. However, they show different discontinuous trends so that 1) and 3) can be ruled out. If the trends of melt-Prg and melt-Mhb have been formed by mixing process, both of those have to show linear trends. However, those trends, especially melt-Prg, show scattered. This observation makes it difficult to consider 4) as the processes that formed the melt-Prg and melt-Mhb trends. Ohta *et al.* (1990) and Ohta & Aoki (1991) have reported that plagioclases in andesite from Yufu Volcano can be divided into two types: anorthite-rich and anorthite-poor, and argued that the Prg and anorthite-rich plagioclase are derived from mafic magma, and Mhb and anorthite-poor plagioclase are derived from felsic magma. Following them, the trends of the Y/Rb and Dy/Rb ratios against the Sr/Rb ratio are shown as vectors for each differentiating mineral (anorthite-rich and -poor plagioclase, Prg and Mhb) in Fig. 11. In both equilibrium and fractional crystallisations, the crystallisations of Prg and anorthite-rich plagioclase, and Mhb and anorthite-poor plagioclase show trends of decreasing Y/Rb and Dy/Rb ratios with decreasing Sr/Rb ratios, which are consistent with trends of melt-Prg and melt-Mhb. Therefore, the trends of melt-Prg and melt-Mhb can be explained by the equilibrium or fractional crystallisations of Prg and anorthite-rich plagioclase, and Mhb and anorthite-poor plagioclase, respectively. From above discussion, it is most plausible to explain in 2). However, from the

Table 3: Calculated partition coefficients of trace-elements between amphibole and melt

Sample	Rb	Nb	La	Ce	Pb	Pr	Sr	Nd	Zr	Sm	Eu	Gd	Tb	Dy	Y	Ho	Er	Tm	Yb	Lu
prg-1	0.241	0.262	0.187	0.326	0.041	0.522	0.406	0.767	0.286	1.24	1.41	1.54	1.60	1.60	1.56	1.54	1.44	1.32	1.20	1.09
prg-2	0.236	0.262	0.157	0.276	0.039	0.445	0.396	0.658	0.262	1.08	1.23	1.35	1.42	1.43	1.40	1.38	1.30	1.20	1.10	1.00
prg-3	0.229	0.254	0.152	0.269	0.045	0.436	0.413	0.649	0.264	1.07	1.23	1.36	1.43	1.44	1.42	1.40	1.32	1.22	1.12	1.02
prg-6	0.215	0.286	0.197	0.348	0.040	0.561	0.373	0.830	0.311	1.35	1.54	1.68	1.76	1.76	1.72	1.69	1.58	1.45	1.32	1.19
prg-8	0.212	0.301	0.177	0.312	0.033	0.503	0.374	0.744	0.280	1.21	1.38	1.51	1.58	1.58	1.54	1.52	1.42	1.31	1.19	1.07
prg-10	0.258	0.239	0.173	0.303	0.044	0.485	0.415	0.713	0.287	1.15	1.31	1.43	1.49	1.48	1.45	1.43	1.34	1.23	1.12	1.01
prg-13	0.276	0.226	0.188	0.324	0.046	0.513	0.442	0.745	0.297	1.18	1.34	1.45	1.50	1.49	1.45	1.42	1.33	1.21	1.10	0.99
prg-14	0.251	0.249	0.190	0.326	0.040	0.514	0.456	0.744	0.279	1.17	1.32	1.42	1.47	1.46	1.42	1.39	1.30	1.19	1.07	0.97
prg-15	0.241	0.283	0.215	0.375	0.051	0.599	0.454	0.878	0.346	1.41	1.61	1.75	1.82	1.81	1.77	1.74	1.63	1.50	1.36	1.23
prg-16	0.226	0.316	0.232	0.402	0.041	0.636	0.421	0.923	0.352	1.46	1.64	1.77	1.82	1.80	1.74	1.71	1.58	1.44	1.29	1.16
prg-17	0.265	0.222	0.191	0.328	0.040	0.518	0.418	0.752	0.280	1.19	1.34	1.45	1.50	1.49	1.45	1.43	1.33	1.21	1.10	0.99
prg-18	0.194	0.390	0.201	0.354	0.036	0.570	0.428	0.841	0.326	1.36	1.56	1.69	1.77	1.76	1.72	1.69	1.58	1.45	1.31	1.19
prg-19	0.261	0.277	0.180	0.317	0.047	0.512	0.436	0.757	0.311	1.24	1.41	1.55	1.62	1.62	1.59	1.57	1.47	1.36	1.23	1.12
prg-20	0.250	0.250	0.144	0.252	0.042	0.405	0.454	0.598	0.244	0.976	1.12	1.23	1.29	1.30	1.28	1.26	1.19	1.10	1.01	0.92
prg-21	0.232	0.296	0.163	0.287	0.044	0.464	0.451	0.688	0.284	1.13	1.30	1.42	1.49	1.50	1.48	1.46	1.37	1.27	1.16	1.05
prg-22	0.243	0.273	0.187	0.327	0.047	0.524	0.436	0.772	0.307	1.25	1.43	1.56	1.63	1.63	1.60	1.57	1.48	1.36	1.24	1.12
mhb-2	0.083	1.665	0.618	1.22	0.033	2.17	0.223	3.49	0.959	6.35	7.51	8.42	8.96	9.05	8.89	8.75	8.17	7.46	6.71	6.00
mhb-3	0.092	1.467	0.584	1.13	0.033	1.97	0.244	3.11	0.907	5.51	6.45	7.16	7.56	7.58	7.41	7.28	6.76	6.15	5.51	4.91
mhb-4	0.088	1.596	0.661	1.30	0.031	2.29	0.209	3.65	1.000	6.56	7.72	8.60	9.09	9.14	8.94	8.78	8.16	7.42	6.64	5.91
mhb-16	0.087	1.669	0.642	1.26	0.033	2.23	0.225	3.57	1.002	6.44	7.58	8.47	8.97	9.02	8.84	8.68	8.08	7.35	6.59	5.88
mhb-33	0.083	1.835	0.735	1.45	0.029	2.59	0.202	4.16	1.065	7.52	8.87	9.89	10.5	10.5	10.3	10.1	9.39	8.52	7.63	6.78

Table 4: Trace-element compositions (ppm) of amphiboles from the Yufu Summit lava

Sample	Rb	Ba	Th	U	Nb	Ta	La	Ce	Pb	Pr	Sr	Nd	Zr	Sm	Hf	Eu	Gd	Tb	Dy	Y	Ho	Er	Tm	Yb	Lu
prg-1	1.81	99.7	0.069	0.035	1.27	0.064	1.80	9.21	1.05	1.41	440	7.82	20.5	2.72	1.16	1.09	3.02	0.450	2.55	12.4	0.550	1.43	0.169	1.20	0.147
prg-2	1.86	108	0.104	0.044	0.87	0.030	2.05	9.23	0.691	1.42	467	8.00	18.7	2.79	0.943	1.04	2.83	0.402	2.43	10.7	0.471	1.20	0.161	0.979	0.111
prg-3	2.49	122	0.114	0.064	1.15	0.087	2.09	10.7	1.00	1.54	460	9.34	17.7	2.85	0.920	1.06	2.68	0.379	2.20	9.40	0.389	1.03	0.145	0.917	0.172
prg-6	1.43	89.7	0.029	0.013	1.38	0.053	1.21	6.27	0.388	1.27	478	7.49	24.6	2.59	1.54	1.12	2.74	0.431	2.63	11.8	0.526	1.40	0.151	1.14	0.109
prg-8	1.51	109	0.078	0.034	0.76	0.027	1.92	9.39	0.741	1.87	534	9.61	17.1	3.08	1.11	1.05	3.13	0.470	2.73	11.8	0.467	1.12	0.184	1.15	0.111
prg-10	2.56	108	0.089	0.022	1.51	0.094	2.35	11.5	0.702	1.89	466	9.18	16.4	2.99	0.969	1.28	2.73	0.409	2.61	11.3	0.554	1.61	0.150	1.20	0.146
prg-13	1.94	122	0.057	0.055	1.10	0.069	1.82	9.54	0.715	1.57	452	8.26	16.3	3.04	0.719	1.19	3.10	0.442	2.84	12.0	0.481	1.27	0.206	1.04	0.145
prg-14	1.91	103	0.085	0.042	1.00	0.056	2.08	9.4	0.645	1.66	487	9.27	19.9	3.20	1.15	1.21	2.98	0.494	2.84	13.8	0.566	1.59	0.173	1.06	0.139
prg-15	2.18	126	0.160	0.038	1.54	0.131	2.44	11.4	0.627	1.89	576	10.2	30.5	2.75	1.26	1.14	2.93	0.387	2.72	12.4	0.464	1.38	0.167	1.13	0.147
prg-16	1.45	101	0.040	0.009	3.22	0.153	2.44	12.1	0.600	2.17	383	13.10	24.6	4.09	1.31	1.63	4.22	0.672	3.95	18.9	0.774	2.11	0.274	1.91	0.234
prg-17	1.48	89.1	0.112	0.037	1.64	0.068	2.96	10.8	0.789	1.33	339	7.74	21.0	2.81	1.15	1.21	2.55	0.433	2.70	12.3	0.548	1.45	0.166	1.00	0.123
prg-18	4.57	170	0.311	0.129	2.79	0.096	5.79	23.1	3.32	3.40	584	18.10	23.0	4.34	0.687	1.30	3.36	0.543	3.17	15.3	0.572	1.63	0.235	1.29	0.164
prg-19	1.35	101	0.078	0.018	1.10	0.059	1.75	7.96	0.568	1.57	526	8.23	25.1	3.05	1.38	1.25	3.13	0.472	2.96	12.7	0.546	1.50	0.188	1.31	0.145
prg-20	1.28	103	0.052	0.012	1.04	0.060	1.61	7.89	0.373	1.47	517	8.31	22.7	3.02	1.28	1.14	2.74	0.467	2.82	12.3	0.469	1.41	0.161	1.10	0.162
prg-21	1.22	90.9	0.021	0.008	1.05	0.043	1.16	6.34	0.311	1.27	466	7.70	15.8	2.83	0.697	1.21	2.93	0.479	2.62	11.7	0.518	1.31	0.168	1.16	0.125
prg-22	1.60	120	0.090	0.013	1.49	0.088	1.65	10.3	0.444	1.77	583	9.71	19.9	2.73	1.05	1.22	3.53	0.426	2.98	11.9	0.423	1.30	0.107	1.23	0.144
mhb-2	2.01	50.3	0.166	0.049	13.70	0.376	13.8	86	0.901	11.80	43.9	54.3	34.7	14.70	2.06	3.34	12.8	2.01	12.4	62.8	2.27	7.03	1.01	6.88	0.823
mhb-3	0.855	48.0	0.641	0.197	10.9	0.302	33.8	131	0.928	16.1	65.9	65.7	28.1	14.1	1.60	3.15	12.8	1.83	10.2	56.9	2.03	6.23	0.911	6.31	0.862
mhb-4	1.00	57.7	0.226	0.055	13.8	0.388	17.3	94.6	0.845	12.8	56.0	57.7	35.5	14.6	1.98	3.19	12.5	1.85	11.9	64.3	2.41	7.16	1.03	6.82	0.992
mhb-16	1.01	50.4	0.137	0.031	13.8	0.396	15.7	98.2	0.843	13.0	44.5	64.1	32.5	16.0	1.86	3.46	15.1	2.25	14.5	73.8	2.86	8.28	1.15	8.31	1.16
mhb-33	0.99	55.4	0.126	0.039	13.6	0.342	14.8	91.7	0.850	12.2	51.4	55.2	36.3	15.1	1.89	3.38	13.0	2.00	12.6	62.2	2.44	6.43	0.955	7.05	0.961

Table 5: Trace-element compositions (ppm) of melt in equilibrium with amphiboles

Sample	Rb	Nb	La	Ce	Pb	Pr	Sr	Nd	Zr	Sm	Eu	Gd	Tb	Dy	Y	Ho	Er	Tm	Yb	Lu
prg-1	7.51	4.86	9.61	28.2	26.0	2.69	1090	10.2	71.7	2.20	0.775	1.97	0.281	1.60	7.96	0.358	0.991	0.128	1.00	0.135
prg-2	7.87	3.30	13.1	33.5	17.9	3.20	1180	12.1	71.1	2.59	0.844	2.09	0.283	1.70	7.61	0.341	0.921	0.134	0.892	0.111
prg-3	10.9	4.53	13.7	39.9	22.1	3.54	1110	14.4	67.1	2.66	0.862	1.98	0.266	1.53	6.67	0.278	0.779	0.118	0.820	0.169
prg-6	6.67	4.82	6.11	18.0	9.68	2.26	1280	9.02	79.3	1.92	0.726	1.63	0.245	1.50	6.90	0.311	0.885	0.104	0.865	0.092
prg-8	7.11	2.53	10.8	30.1	22.2	3.72	1430	12.9	61.0	2.55	0.759	2.08	0.298	1.73	7.62	0.308	0.784	0.141	0.965	0.103
prg-10	9.95	6.30	13.6	38.0	15.9	3.90	1120	12.9	57.0	2.60	0.977	1.91	0.275	1.76	7.75	0.388	1.21	0.122	1.07	0.145
prg-13	7.03	4.85	9.71	29.4	15.5	3.07	1020	11.1	54.6	2.57	0.891	2.14	0.295	1.91	8.28	0.338	0.955	0.169	0.950	0.146
prg-14	7.63	4.00	10.9	28.8	16.3	3.23	1070	12.5	71.3	2.74	0.920	2.09	0.335	1.94	9.70	0.406	1.23	0.146	0.992	0.144
prg-15	9.07	5.42	11.4	30.5	12.2	3.15	1270	11.6	88.3	1.95	0.711	1.67	0.213	1.50	6.99	0.266	0.848	0.111	0.830	0.119
prg-16	6.42	10.2	10.5	30.1	14.7	3.41	910	14.2	69.9	2.81	0.993	2.39	0.369	2.20	10.8	0.453	1.34	0.190	1.47	0.202
prg-17	5.57	7.39	15.5	32.9	19.6	2.57	813	10.3	75.0	2.36	0.903	1.76	0.288	1.81	8.50	0.385	1.09	0.137	0.910	0.124
prg-18	23.6	7.17	28.8	65.2	92.8	5.97	1360	21.5	70.7	3.19	0.834	1.98	0.308	1.80	8.87	0.338	1.03	0.162	0.981	0.138
prg-19	5.18	3.98	9.73	25.1	12.0	3.06	1210	10.9	80.8	2.47	0.882	2.02	0.291	1.82	7.98	0.348	1.02	0.139	1.06	0.130
prg-20	5.11	4.15	11.2	31.3	8.84	3.64	1140	13.9	93.0	3.09	1.02	2.23	0.362	2.17	9.61	0.372	1.18	0.146	1.09	0.176
prg-21	5.29	3.55	7.08	22.1	7.07	2.74	1040	11.2	55.4	2.51	0.932	2.06	0.320	1.74	7.89	0.356	0.953	0.132	0.999	0.119
prg-22	6.58	5.46	8.81	31.4	9.47	3.38	1340	12.6	64.8	2.18	0.856	2.26	0.261	1.83	7.44	0.269	0.881	0.078	0.992	0.128
mhb-2	24.3	8.22	22.4	70.5	27.6	5.44	197	15.5	36.2	2.31	0.445	1.52	0.225	1.37	7.06	0.260	0.861	0.135	1.02	0.137
mhb-3	9.32	7.42	57.8	116	27.8	8.14	270	21.1	31.0	2.56	0.488	1.78	0.242	1.35	7.68	0.278	0.921	0.148	1.15	0.175
mhb-4	11.3	8.65	26.2	73.0	27.2	5.59	268	15.8	35.5	2.23	0.413	1.45	0.204	1.30	7.19	0.274	0.878	0.138	1.03	0.168
mhb-16	11.6	8.25	24.5	77.9	25.5	5.84	198	17.9	32.4	2.48	0.456	1.79	0.251	1.60	8.36	0.329	1.02	0.157	1.26	0.197
mhb-33	11.9	7.42	20.1	63.0	29.3	4.72	254	13.3	34.1	2.01	0.381	1.31	0.191	1.20	6.04	0.241	0.684	0.112	0.924	0.142

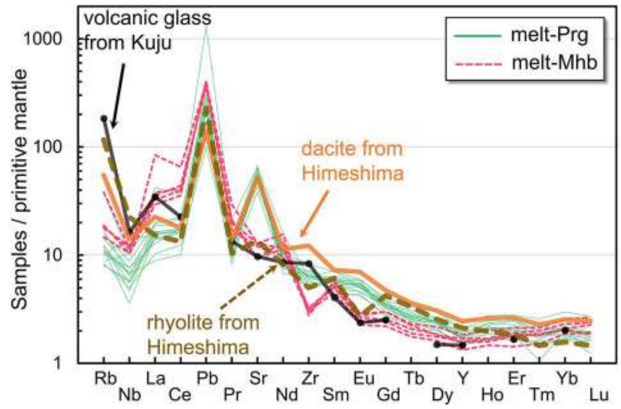

Fig. 9. Primitive-mantle-normalised trace-element patterns for estimated melts in equilibrium with amphiboles. Dacite and rhyolite from the Himeshima volcanic group (Shibata *et al.*, 2014) and volcanic glass from the Kuju volcanic group (Albert et al., 2019) are also shown for comparison. The normalisation values are from Sun & McDonough (1989).

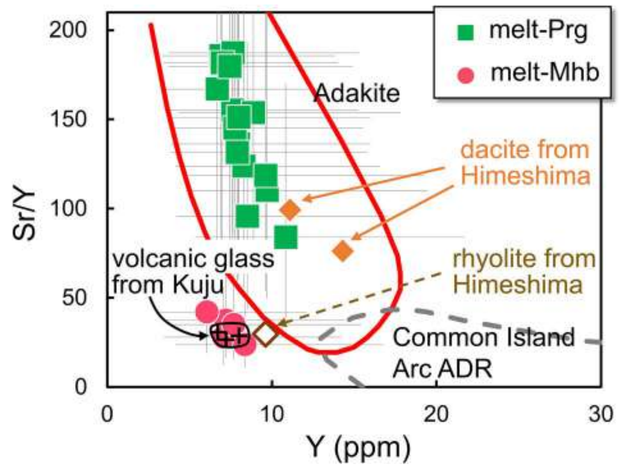

Fig. 10. Sr/Y versus Y diagram for estimated melts in equilibrium with amphiboles. Data for dacite and rhyolite from the Himeshima volcanic group are from Shibata *et al.* (2014) and for volcanic glass from the Kuju volcanic group are from Albert et al. (2019). The compositional ranges of common island-arc ADR (andesite, dacite, and rhyolite) and adakite are from Defant & Drummond (1990). The gray bars for melt-Prg and melt-Mhb are error bars.

existence of amphiboles recording the changes of melt composition in Yufu Summit lava, equilibrium crystallisation is more preferred than fractional crystallisation, even if the closed-system was incomplete. Saito *et al.* (2001) reported that the whole-rock of rhyolites from Satsuma-Iwoujima volcano, which is located to the south of Kyushu Island, Japan, have similar major-element compositions regardless of the eruption period, whereas the SiO_2 content of plagioclase-hosted melt inclusions and matrix glass in them increase with time. It is considered that this temporal change can be explained by the plagioclase crystallisation within the magma chamber (Saito *et al.*, 2001). In a similar manner, the two end-member magmas that formed Yufu Summit lava might have changed only in melt compositions though the crystallisation of plagioclase and amphibole, without changing the composition of the bulk rock.

Geochemical characteristics of end-member magmas of the Yufu volcano andesite

From the estimated *P*, *T*, and major- and trace-element compositions of melt-Prg and melt-Mhb, it can be suggested that the Prg and Mhb coexisted in Yufu Summit lava by mixing of magmas containing those melts, respectively. The chemical variations of melt-Prg and melt-Mhb suggest that possibility that the chemical compositions of those melts changed by the crystallisation of Prg, Mhb and plagioclase before magma mixing. On the other hand, it can be considered that the bulk composition of end-member magmas containing those melts, respectively, could be unchanged. However, the geochemical features of end-member magmas are still unclear. It is difficult to characterise the geochemistry of end-member magmas produced by magma mixing. Consequently, the magmas that plot along extensions of the mixing line on a biaxial diagram of the whole-rock composition of magma have previously been assumed to be end-member magmas. Candidates for end-member magmas are often chosen from mixed magmas themselves or from magmas of neighbouring volcanoes, even from those that are not directly geologically related (e.g. Ohta & Aoki, 1991). Therefore, most previous studies have only roughly estimated (or assumed) the chemical compositions of end-member magmas because of the difficulties of constraining their nature and origin.

As magma is a mixture of minerals and melt, the chemical composition of magma can be calculated by the mixing

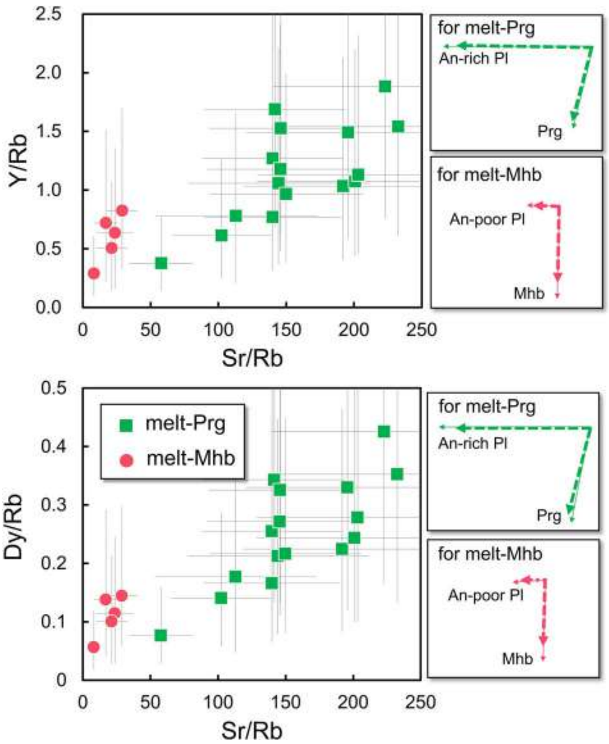

Fig 11. Y/Rb versus Sr/Rb and Dy/Rb versus Sr/Rb diagrams for estimated melts in equilibrium with amphiboles. Gray bars for melt-Prg and melt-Mhb are error bars. The *Kds* used for differentiation vectors in this study are shown Supplementary Table 4. The *Kds* may vary during the crystallisation in each melt, but we assume constant for such changes. The dashed and solid arrows represent equilibrium and fractional crystallisation, respectively. The vectors of each mineral are in the case of 30% differentiation.

relationship inferred from the chemical compositions of minerals and melt, as described here. Ohta *et al.* (1990) reported the mineral assemblage of andesite from Yufu Volcano as comprising olivine (Ol), quartz (Qz), clinopyroxene (Cpx), orthopyroxene (Opx), Prg, Mhb, biotite (Bt), anorthite (An)-rich and An-poor plagioclase (Pl), and opaque minerals. It has been proposed that the Ol, Cpx, Prg, and An-rich Pl were derived from a mafic magma, whereas the Qz, Opx, Mhb, An-poor Pl, and Bt were crystallised from a felsic magma (Ohta *et al.*, 1990; Ohta & Aoki, 1991). Major-element compositions of those phenocrysts, except for Qz, have been reported by Ohta *et al.* (1990), and the major-element composition of Qz can be assumed as $SiO_2 = 100$ wt %.

We estimated the chemical compositions of the end-member magmas on a biaxial plot of SiO_2 versus Y (Fig. 12). This approach is taken because, as described below, the Y contents in phenocrysts, except for Cpx and Opx, can be assumed to be zero, which simplifies the estimation. The *Kd* value of Y between Pl and melt is 0.004 to 0.037 for $SiO_2 = 52$ to 60 wt % in melt (e.g. Bindeman & Davis, 2000; Dohmen & Blundy, 2014) and 0.01 to 0.03 for $SiO_2 > 70$ wt % in melt (e.g. Padilla & Gualda, 2016 and references therein; Iveson *et al.*, 2018). These values of *Kd*s allow us to assume that the contents of Y in An-rich and An-poor Pl are zero. Similarly, we assume that the contents of Y in Ol, Bt, and Qz are also zero because Ol and Qz incorporate negligible Y (e.g. Peppard *et al.*, 2001; Evans *et al.*, 2008), and the *Kd* value between Bt and rhyolite melt is quite low (0.02–0.047) (Bachmann *et al.*, 2005; Padilla & Gualda, 2016). Because the *Kd* value of Y between Cpx and melt is 0.18 to 1.08, for the case where the SiO_2 content of melt is 52 to 60 wt % (Bédard, 2014 and references therein), the Y content of Cpx can be estimated as 1.5 to 8.8 ppm, as shown in Fig. 12. The *Kd* value of Y between Opx and rhyolite melt is 0.14 to 0.99 (Brophy *et al.*, 2011; Czuppon *et al.*, 2012), giving an estimated Y content in Opx of 1.0 to 7.2 ppm (Fig. 12). The major- and trace-element compositions of Prg and Mhb in Fig. 12 are as measured in this study. Furthermore, we estimated the major- and trace-element compositions of melt equilibrated with amphibole phenocrysts in the mafic and felsic magmas, respectively. Therefore, it should be possible to determine the chemical characteristics of the mafic and felsic end-members by the mixing relationship between minerals and melts, as discussed below.

The mixing relationship between minerals and melts is shown in Fig. 12 for the case of SiO_2 and Y concentrations. The area bounded by lines connecting Prg, An-rich Pl, Cpx, and melt-Prg in Fig. 12 shows the compositional range of magma that can be produced by mixing Prg, An-rich Pl, Cpx, and melt-Prg with respect to SiO_2 and Y concentrations of the mafic end-member. The mafic end-member also contains Ol as phenocrysts, but the modal composition of Ol is very small, up to 0.2 vol % in andesite (Ohta *et al.*, 1990). Therefore, even if 1 vol % of Ol is added to the estimation, the mafic end-member region is affected only by a slight shift of the line connecting Prg and An-rich Pl towards lower SiO_2. The SiO_2 and Y concentrations of the mafic end-member should plot in this area bounded by lines connecting Prg, An-rich Pl, Cpx, and melt-Prg. The mixing relationship between Mhb, An-poor Pl, Opx, and melt-Mhb is also shown in Fig. 12. The SiO_2 and Y concentrations of the felsic end-member should plot in this area bounded by line connecting Mhb, An-poor Pl, Opx, and melt-Mhb. The felsic end-member also contains Bt and Qz as phenocrysts, but the modal compositions of these minerals are very small in andesite, up to 0.1 vol % and 1 vol %, respectively, (Ohta *et al.*, 1990). Therefore, even if 1 vol % Bt and Qz are added to the estimation, then the felsic end-member region is affected only by a slight expansion towards low SiO_2 and high SiO_2, respectively.

From the discussion above, the compositional ranges of mafic and felsic end-members are constrained by the polygonal areas in the plane of SiO_2 and Y concentrations. However, the range in compositions is still too wide to clarify the geochemical characteristics of each end-member, and an additional constraint is needed. Magma mixing has been conventionally interpreted from

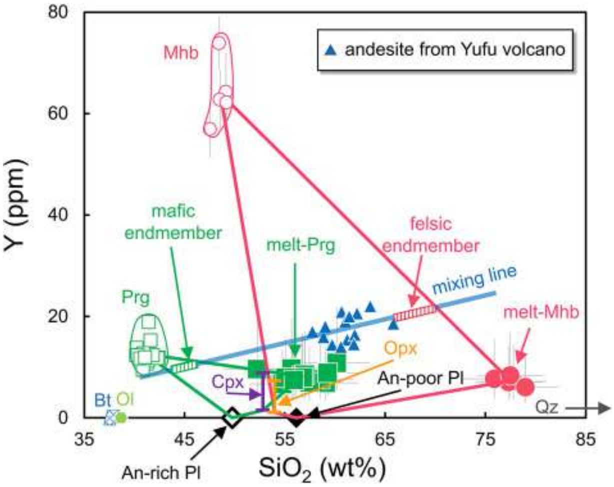

Fig 12. Estimation of the geochemistry of the end-member magmas of Yufu Volcano andesite based on the relationship between Y and SiO_2. The SiO_2 contents of anorthite (An)-rich plagioclase (Pl) (open diamond), An-poor Pl (solid diamond), clinopyroxene (Cpx; purple bar), orthopyroxene (Opx; orange bar), olivine (Ol; yellow-green hexagon), and biotite (Bt; mesh rhombus) are from Ohta *et al.* (1990). The SiO_2 content of quartz (Qz) is assumed to be 100 wt %. The Y contents of An-rich Pl and An-poor Pl, Ol, Bt, and Qz are assumed to be zero (see the text for details in 'Geochemical characteristics of end-member magmas of the Yufu Volcano andesite'). The Y contents of Cpx and Opx are assumed as 1.5 to 8.8 and 1.0 to 7.2 ppm, respectively (see the text for details in 'Geochemical characteristics of end-member magmas of the Yufu Volcano andesite'). Green and pink quadrangles indicate the ranges of four-component mixing of pargasite (Prg), melt-Prg, An-rich Pl, and Cpx, and of magnesio-hornblende (Mhb), melt-Mhb, An-poor Pl, and Opx, respectively. The blue line is the regression line of whole-rock compositions of andesite from Yufu Volcano (Ohta & Aoki, 1991; Sugimoto *et al.*, 2006; this study) represents the mixing line. The striped green rectangle represents the intersection of the green polygonal area and the blue line. The striped pink rectangle similarly shows pink polygonal area and the blue line. The gray bars are error bars. Some error bars are smaller than the symbols.

linear trends in bivariate plots of whole-rock geochemical data (e.g. Sakuyama, 1981; Koyaguchi, 1986; Clynne, 1999). The whole-rock composition of andesite from Yufu Volcano also shows linear trends in bivariate diagrams, which are explained by the mixing of mafic and felsic end-member magmas (Ohta *et al.*, 1990; Ohta & Aoki, 1991). Figure 12 shows the relationship between whole-rock Y and SiO_2 contents of andesite from Yufu Volcano (Ohta & Aoki, 1991; Sugimoto *et al.*, 2006; Table 6). The regression line represents the mixing line (Fig. 12), and the mafic and felsic end-member magmas must accordingly plot on this mixing line. Therefore, we have successfully constrained the end-member magmas in two different ways, giving us additional confidence that the characterisations of the end-member magmas are robust. The areas where the mixing line passes within the polygonal areas can be considered as the mafic and felsic end-member magmas, which are labelled in Fig. 12 and depicted as striped domains. The cut-off for the low-SiO_2 end of felsic end-member magma is most silicic andesite sample from Yufu Volcano ($SiO_2 = 65.83$ wt %; Sugimoto *et al.*, 2006). The ranges of SiO_2 and Y in the striped domains are 44 to 47 wt % and 9 to 12 ppm for the mafic end-member magma, and 66 to 70 wt % and 19 to 22 ppm for the felsic end-member magma, respectively. Herein, we refer to the mafic and felsic end-member magmas estimated in this study as 'Mafic-EM' and 'Felsic-EM', respectively. The median values of the compositional ranges of SiO_2 and Y for Mafic-EM and Felsic-EM are ≈45 wt % and ≈10 ppm, and ≈68 wt % and ≈21 ppm, respectively.

Table 6: Whole-rock geochemical compositions of volcanic rocks and mafic inclusions from Yufu volcano and Jissoji volcano, respectively

	Andesite from Yufu volcano				Mafic inclusion from Yufu volcano			Jissoji
Sample	YT-03	YT-05	YT-04	05040405	IKin1	IKin2	IKin3	
Unit	Yun	Ys	Ki	Ik	Ik	Ik	Ik	
wt %								
SiO_2	60.62	61.90	61.97	61.24	52.42	53.54	55.18	64.79**
TiO_2	0.72	0.73	0.71	0.77	1.06	0.94	0.95	
Al_2O_3	17.02	16.38	16.49	16.20	18.14	18.04	17.50	
FeO*	6.07	5.71	5.61	5.82	8.15	7.81	7.59	
MnO	0.13	0.13	0.13	0.13	0.15	0.15	0.15	
MgO	2.99	2.84	3.16	3.00	5.16	4.77	4.52	
CaO	6.59	6.16	5.96	6.35	9.98	9.63	8.77	
Na_2O	3.46	3.46	3.45	3.46	3.05	3.14	3.05	
K_2O	1.56	1.92	1.85	1.83	0.85	0.99	1.29	
P_2O_5	0.13	0.11	0.17	0.12	0.14	0.14	0.15	
total	99.28	99.33	99.49	98.91	99.09	99.13	99.16	
ppm								
Cs	1.17	1.97	1.10	1.84	0.623	1.09	0.939	2.29
Rb	42	54	48	50	20	27	32	66**
Ba	407	534	516	468	216	233	297	627**
Th	4.04	5.06	4.80	4.93	1.63	1.69	2.63	6.24
U	0.888	1.10	1.05	1.07	0.386	0.507	0.602	1.35
Nb	8	9	10	9	5	6	8	11**
La	12.4	14.0	15.9	13.6	7.64	8.37	10.6	18.3
Ce	25.3	28.2	32.4	28.2	17.7	18.9	23.3	35.5
Pb	6.75	8.10	8.06	7.81	3.64	3.72	5.54	10.1
Pr	2.86	3.21	3.73	3.29	2.39	2.49	2.96	4.02
Sr	483	454	494	462	538	494	520	475**
Nd	11.6	12.8	15.2	13.4	11.4	11.5	13.3	15.6
Zr	94	114	125	110	56	60	71	130**
Sm	2.49	2.75	3.21	2.87	2.95	2.91	3.22	3.06
Eu	0.938	0.970	1.12	1.02	1.05	1.03	1.09	1.00
Gd	2.72	2.97	3.42	3.11	3.23	3.20	3.49	3.30
Tb	0.387	0.408	0.477	0.438	0.484	0.475	0.501	0.432
Dy	2.37	2.46	2.83	2.59	2.95	2.92	3.08	2.55
Y	14.0	14.7	16.4	15.4	16.3	16.4	17.1	15.1
Ho	0.484	0.502	0.562	0.531	0.585	0.585	0.609	0.506
Er	1.49	1.56	1.74	1.63	1.75	1.75	1.82	1.58
Tm	0.218	0.224	0.259	0.234	0.243	0.247	0.261	0.231
Yb	1.50	1.58	1.77	1.64	1.63	1.65	1.72	1.60
Lu	0.229	0.237	0.266	0.240	0.233	0.234	0.253	0.240

*Total Fe as FeO. ** The contents of SiO_2, Rb, Ba, Nb, Sr, and Zr of dacite from Jissoji are from Ohta & Aoki (1991). The units of Yufu main body lava (Ys), Yunotsubo lava (Yun), Kitainoseto lava (Ki), and Ikeshiro lava (Ik) are from Ohta et al. (1990).

Magma mixing results in linear trends in Harker diagrams for most major- and trace-elements (Ohta *et al.*, 1990; Ohta & Aoki, 1991). Above, we determined the SiO_2 concentrations of Mafic-EM and Felsic-EM, which in turn allows us to estimate the concentrations of major- and trace-elements of these end-member magmas from linear trends in Harker diagrams. We first approximated the Harker diagram data for each element by a linear trend using ordinary least square regression and calculating the correlation coefficient (*R*). We judged that the elements for which the value of *R* ranges between −0.3 and + 0.3, such as P_2O_5, Sm, Gd, Tm, Yb, and Lu (Fig. 13a), show no correlation in Harker diagrams and are excluded from the discussion below. This is because the R-value between 0.3 and − 0.3 is conventionally considered uncorrelated. Next, the concentrations of each element were estimated for $SiO_2 = 45$ wt % (Mafic-EM) and $SiO_2 = 68$ wt % (Felsic-EM) using the linear approximations describe above. Harker diagrams for whole-rock Ba and Sr contents of andesites from Yufu Volcano (Ohta & Aoki, 1991; Sugimoto *et al.*, 2006; Table 6) are shown in Fig. 13b and c as examples. The relationships between Ba and SiO_2 and between Sr and SiO_2 have *R*-values and p-values of 0.81 and 0.0004, and − 0.74 and 0.0023, respectively, both of which are statistically significant. The calculated concentrations of Ba and Sr of Mafic-EM and Felsic-EM are 100 and 820, and 620 and 350 ppm, respectively. In the same way, we estimated the concentration of each of the other elements, which are shown in Table 7, in the Mafic-EM and Felsic-EM from linear equations of the relationships between these other elements and SiO_2.

The calculated concentrations of major- and trace-elements in Mafic-EM and Felsic-EM are given in Table 7, and the PM patterns of calculated trace-element concentrations of the end-member magmas are presented in Fig. 14. The PM pattern of Mafic-EM shows a zigzag pattern from Rb to Nd, together with enrichment in alkali and alkali-earth elements (Rb, Ba, and Sr) (Fig. 14). In contrast, Felsic-EM is characterised by a pattern that is typical of subduction-zone magmas, with a negative Nb anomaly, enrichment in LILEs, and a weak positive Sr anomaly. Ohta & Aoki (1991)

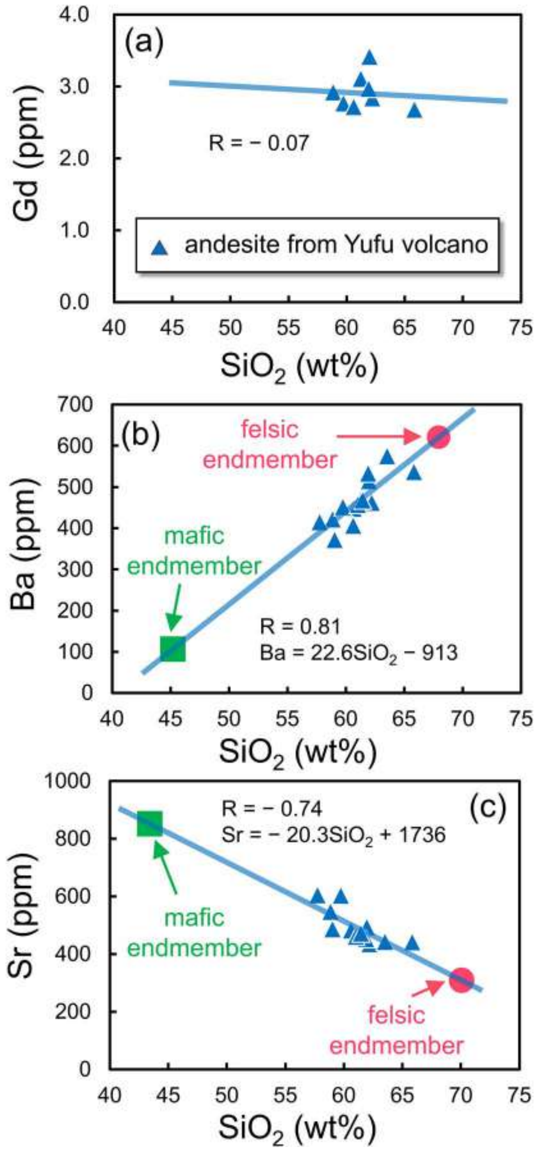

Fig 13. Diagrams of (a) Gd versus SiO_2, (b) Ba versus SiO_2, and (c) Sr versus SiO_2 as examples of estimating other element (excluding SiO_2 and Y) compositions of end-member magmas. Data for whole-rock compositions of andesite from Yufu Volcano and the blue line are the same as in Fig. 12. The *R*-value is the correlation coefficient. Linear regression equations for the respective relationships are given in (b) and (c). The green square and pink circle in (b) and (c) indicate the compositions of the mafic and felsic end-member magmas, respectively, calculated by substituting the SiO_2 concentration estimated in Fig. 12 into the respective regression equations. Symbols exceed the size of error bars.

argued that the mafic and felsic end-members could be represented by mafic inclusions that are contained in andesite from Yufu Volcano and dacite from an adjacent older volcano (Jissoji Volcano), respectively, on the basis of the whole-rock chemical and Sr isotopic compositions of andesites and mafic inclusions from Yufu Volcano, and dacite from Jissoji Volcano. Therefore, we compared the chemical compositions of the end-member magmas proposed by Ohta & Aoki (1991) (i.e. mafic inclusions from Yufu Volcano and dacite from Jissoji Volcano; Table 6) with the end-members estimated in this study (i.e. Mafic-EM and Felsic-EM; Table 7), as follows.

Table 7: Chemical compositions of estimated end-member magmas

	Mafic endmember	Felsic endmember
wt %		
SiO_2	45	68
TiO_2	1.4	0.43
Al_2O_3	18	16
FeO*	11	3.6
MnO	0.17	0.11
MgO	6.6	1.6
CaO	12	3.8
Na_2O	3.1	3.6
K_2O	0.57	2.3
ppm		
Rb	5.2	67
Ba	100	620
Th	0.33	6.9
U	0.17	1.5
Nb	4.0	11
La	0.86	19
Ce	7.7	36
Pb	0.63	11
Pr	1.1	4.2
Sr	820	350
Nd	7.8	15
Zr	78	130
Eu	1.1	0.91
Tb	0.50	0.39
Dy	3.2	2.3
Y	10	21
Ho	0.65	0.46
Er	1.9	1.5

*Total Fe as FeO

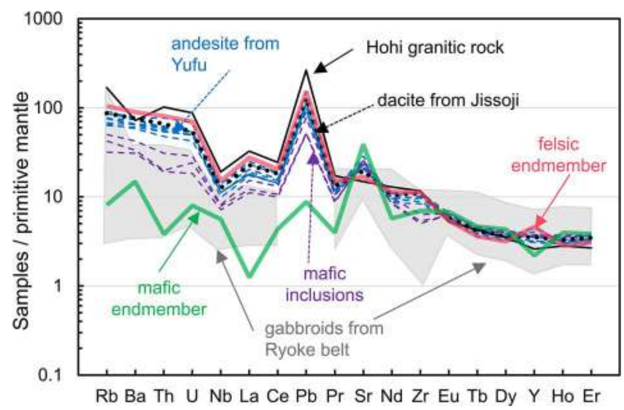

Fig 14. Primitive-mantle-normalised trace-element patterns of end-member magmas. Data for andesites and, mafic inclusions from Yufu Volcano are from Sugimoto *et al.* (2006) and this study, for dacite from Jissosi Volcano are Ohta & Aoki (1991) and this study, for averaged granitic rocks from the Hohi area are from Kamei *et al.* (2009) and gabbroids from the Ryoke belt are from Takagi *et al.* (2010). The normalising values are from Sun & McDonough (1989).

The PM pattern of the Mafic-EM is dissimilar to that of Yufu mafic inclusion, with the Mafic-EM having markedly lower concentrations of Rb, Ba, Th, U, Pb, light REEs, and Y, and higher concentrations of Sr relative to the mafic inclusions (Fig. 14). These differences indicate that the mafic inclusions are unlikely to represent the mafic end-member. The PM pattern of dacite of Jissoji Volcano shows typical features of island-arc magmas,

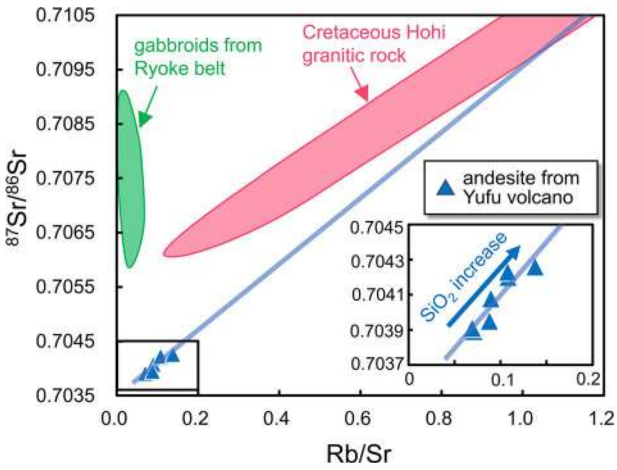

Fig. 15. Rb/Sr versus $^{87}Sr/^{86}Sr$ diagram for the whole-rocks of andesite from Yufu Volcano, gabbroid from the Ryoke belt, and Cretaceous Hohi granitic rocks. Data for whole-rocks of andesite from Yufu Volcano are from Ohta & Aoki (1991) and Sugimoto *et al.* (2006), for gabbroid from Ryoke belt are from Kagami *et al.* (2000) and Okano *et al.* (2000), and for Cretaceous Hohi granitic rocks are from Osanai *et al.* (1990). The blue line is the regression line of whole-rock of andesite from Yufu volcano (Ohta & Aoki, 1991; Sugimoto *et al.*, 2006).

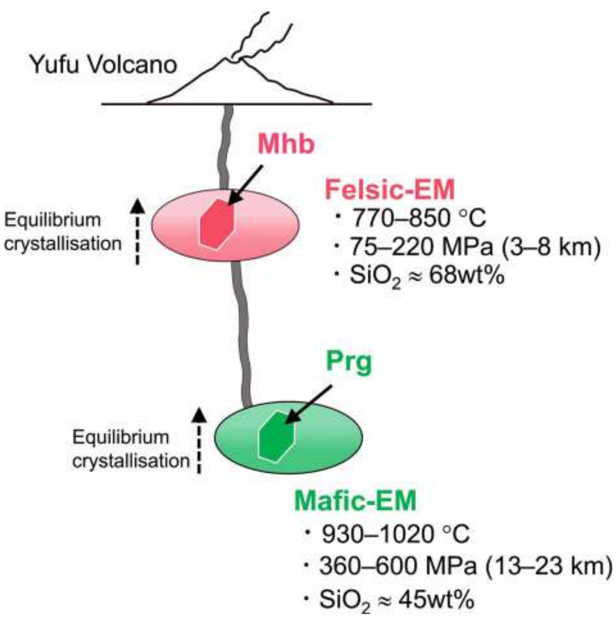

Fig. 16. A schematic illustration of the magma plumbing system for Yufu Volcano. Mafic- and felsic-endmembers (EMs), in which pargasite (Prg) and magnesio-hornblende (Mhb) crystallised, respectively, existed beneath Yufu Volcano at different temperature, depth and chemical composition. These magmas underwent changes in their melt compositions though equilibrium crystallisation of amphibole and plagioclase, and subsequently were mixed to form andesitic magma of Yufu Volcano.

including a weak positive Sr spike, which are similar to the features of the Felsic-EM estimated in this study (Fig. 14). These similarities demonstrate that the chemical composition of the estimated felsic end-member in this study is consistent with the felsic end-member proposed by Ohta & Aoki (1991); i.e. dacite of Jissoji Volcano.

It is considered that rocks of the Ryoke belt could occur beneath Yufu Volcano (e.g. Wallis *et al.*, 2020), along with Cretaceous granitic rocks of the Beppu–Shimabara graben (Hoshizumi *et al.*, 1988). The PM patterns of gabbroids from Ryoke belt (Takagi *et al.*, 2010) and Cretaceous Hohi granitic rocks exposed in the Beppu-Shimabara graben (Kamei *et al.*, 2009) are also shown in Fig. 14. Additionally, the $^{87}Sr/^{86}Sr$ ratios of whole-rocks of andesite from Yufu Volcano (Ohta & Aoki, 1991; Sugimoto *et al.*, 2006), gabbroids from Ryoke belt (Kagami *et al.*, 2000; Okano *et al.*, 2000) and Cretaceous Hohi granitic rocks (Osanai *et al.*, 1990) are plotted against Sr/Rb ratios in Fig. 15. The PM pattern of the Mafic-EM plots within the range of gabbroids from the Ryoke belt, except for La and Pb (Fig. 14). On the other hand, the gabbroids from Ryoke belt show significantly higher $^{87}Sr/^{86}Sr$ ratios than the whole-rocks of andesite from Yufu Volcano (Fig. 15). This observation makes it difficult to assume the gabbroid from Ryoke belt as a source of Mafic-EM. However, if it can be hypothesised that the crustal materials beneath Yufu Volcano have similar trace-element compositions to the gabbroids from Ryoke belt, as well as lower Sr isotopic ratios than them resulting from younger igneous activity, the similarity in trace-element compositions of Mafic-EM and gabbroids from Ryoke belt (Fig. 14) could be explained by assuming that such crustal materials are one of the sources of Mafic-EM. Further investigations are needed to determine whether such crustal materials exist beneath Yufu Volcano.

The Felsic-EM shows a similar PM pattern to that of the Cretaceous Hohi granitic rocks (Fig. 14). In Fig. 15, the $^{87}Sr/^{86}Sr$ and Rb/Sr ratios of Cretaceous Hohi granitic rocks are higher than those of whole-rocks of andesite from Yufu Volcano. The $^{87}Sr/^{86}Sr$ ratios in the whole-rocks of andesite from Yufu Volcano increase with increasing Rb/Sr ratios and SiO_2 content (Fig. 15; Ohta & Aoki, 1991). The composition range of Cretaceous Hohi granitic rocks is plotted on an extension of the high-Rb/Sr and SiO_2 side of trend in the whole-rocks of andesite from Yufu Volcano (Fig. 15). From these observations, it can be suggested the possibility that the Cretaceous Hohi granitic rocks contribute to Felsic-EM.

Summary

We analysed the major- and trace-element compositions of amphibole in Yufu Summit lava, and then determined *P*, *T*, and major- and trace-element compositions of the two precursor end-member magmas prior to mixing (Fig. 16). Furthermore, we show that the major- and trace-element compositions of amphiboles can directly identified the chemical composition of end-member magmas by estimating the possible compositional range of the magmas from the mixing relationships between minerals (amphibole, Pl, Cpx, and Opx) and melt compositions, on the basis that magma is a mixture of minerals and melt, and combining this information with the mixing trends of whole-rock compositions. Our results reveal that the major- and trace-element compositions of amphibole can be used to elucidate the genesis of magma that has undergone complicated processes such as magma mixing. Amphibole-bearing volcanic rocks are found in various arcs around the Pacific Ocean, including the Cascades, Andes, Indonesia, and Aleutians chains, as well as Japan (e.g. Sakuyama, 1983). Therefore, the principles and method of our study should be widely applicable to amphiboles from other volcanoes and are expected to provide new insights into magmatic evolution that have been hitherto difficult to obtain from whole-rock compositions.

FUNDING

This work was supported by research grants from JSPS KAKENHI [25400512 to T.S.], the Fukada Geological Institute [Fukada Grant-in-Aid to I.O.], JST SPRING [JPMJSP2132 to I.O.], Oita Prefecture

Hot Spring Research Group, and Hiroshima Institute of Plate Convergence Region Research, Hiroshima University.

DATA AVAILABILITY STATEMENT

The data underlying this article are available in the article and in its online supplementary material.

ACKNOWLEDGEMENTS

We are grateful to T. Hirayama, B. Dey, R. Fujiwara, K. Das, and M. Miyahara for their many contributions to this study. We are sincerely thankful to the technical support of the Natural Science Centre for Basic Research and Development, Hiroshima University in EPMA analysis. We are grateful to K. Takemura for his encouragement during this study, and T.M. Chakraborti for improving the manuscript. We wish to the thank I. Miyagi for his support in writing the manuscript. We also greatly appreciate the helpful comments provided by G.F. Cooper, A. Langone, and an anonymous reviewer. A. Kent and G. Zellmer are deeply acknowledged for their editorial works and constructive comments.

References

Albert, P. G., Smith, V. C., Suzuki, T., McLean, D., Tomlinson, E. L., Miyabuchi, Y., Kitaba, I., Mark, D. F., Moriwaki, H., SG06 Project Members & Nakagawa, T. (2019). Geochemical characterisation of the Late Quaternary widespread Japanese tephrostratigraphic markers and correlations to the Lake Suigetsu sedimentary archive (SG06 core). *Quaternary Geochronology* **52**, 103–131. https://doi.org/10.1016/j.quageo.2019.01.005.

Anderson, J. L. & Smith, D. R. (1995). The effects of temperature and f_{O2} on the Al-in-hornblende barometer. *American Mineralogist* **80**, 549–559. https://doi.org/10.2138/am-1995-5-614.

Anderson, A. T., Newman, S., Williams, S. N., Druitt, T. H., Skirius, C. & Stolper, E. (1989). H_2O, CO_2, CI, and gas in Plinian and ash-flow bishop rhyolite. *Geology* **17**, 221–225. https://doi.org/10.1130/0091-7613(1989)017<0221:HOCCAG>2.3.CO;2.

Bachmann, O., Dungan, M. A. & Busy, F. (2005). Insights into shallow magmatic processes in large silicic magma bodies: the trace element record in the fish canyon magma body, Colorado. *Contributions to Mineralogy and Petrology* **149**, 338–349. https://doi.org/10.1007/s00410-005-0653-z.

Bédard, J. H. (2014). Parameterizations of calcic clinopyroxene—melt trace element partition coefficients. *Geochemistry, Geophysics, Geosystems* **15**, 303–336. https://doi.org/10.1002/2013GC005112.

Bindeman, I. N. & Davis, A. M. (2000). Trace element partitioning between plagioclase and melt: investigation of dopant influence on partition behavior. *Geochimica et Cosmochimica Acta* **64**, 2863–2878. https://doi.org/10.1016/S0016-7037(00)00389-6.

Bindeman, I. N., Leonov, V. L., Izbekov, P. E., Ponomerva, V. V., Watts, K. E., Shipley, N. K., Perepelov, A. B., Bazanova, L. I., Jicha, B. R., Singer, B. S., Schmitt, A. K., Portnyagin, M. V. & Chen, C. H. (2010). Large-volume silicic volcanism in Kamchatka: Ar–Ar and U–Pb ages, isotopic, and geochemical characteristics of major pre-Holocene caldera-forming eruptions. *Journal of Volcanology and Geothermal Research* **189**, 57–80. https://doi.org/10.1016/j.jvolgeores.2009.10.009.

Blundy, J. D. & Holland, T. J. B. (1990). Calcic amphibole equilibria and a new amphibole-plagioclase geothermometer. *Contributions to Mineralogy and Petrology* **104**, 208–224. https://doi.org/10.1007/BF00306444.

Blundy, J. D. & Holland, T. J. B. (1992). 'Calcic amphibole equilibria and a new amphibole-plagioclase geothermometer': reply to the comments of Hammarstrom and Zen, and Rutherford and Johnson. *Contributions to Mineralogy and Petrology* **111**, 269–272. https://doi.org/10.1007/BF00348959.

Blundy, J. D. & Wood, B. J. (1994). Prediction of crystal–melt partition coefficients from elastic moduli. *Nature* **372**, 452–454. https://doi.org/10.1038/372452a0.

Brophy, J. G., Ota, T., Kunihiro, T., Tsujimori, T. & Nakamura, E. (2011). In situ ion-microprobe determination of trace element partition coefficients for hornblende, plagioclase, orthopyroxene, and apatite in equilibrium with natural rhyolitic glass, little Glass Mountain rhyolite, California. *American Mineralogist* **96**, 1838–1850. https://doi.org/10.2138/am.2011.3857.

Chang, Q., Shibata, T., Shinotsuka, K., Yoshikawa, M. & Tatsumi, Y. (2003). Precise determination for trace elements in geological standard rocks using inductively coupled plasma mass spectrometry (ICPMS). *Frontier Research on Earth Evolution* **1**, 357–360.

Chertkoff, D. G. & Gardner, J. E. (2004). Nature and timing of magma interactions before, during, and after the caldera-forming eruption of Volcán Ceboruco, Mexico. *Contributions to Mineralogy and Petrology* **146**, 715–735. https://doi.org/10.1007/s00410-003-0530-6.

Clynne, M. A. (1999). A complex magma mixing origin for rocks erupted in 1915, Lassen Peak, California. *Journal of Petrology* **40**, 105–132. https://doi.org/10.1093/petroj/40.1.105.

Cooper, G. F. & Wilson, C. J. N. (2014). Development, mobilisation and eruption of a large crystal-rich rhyolite: the Ongatiti ignimbrite, New Zealand. *Lithos* **198-199**, 38–57. https://doi.org/10.1016/j.lithos.2014.03.014.

Czuppon, G., Lukács, R., Harangi, S., Mason, P. R. D. & Ntaflos, T. (2012). Mixing of crystal mushes and melts in the genesis of the Bogács ignimbrite suite, northern Hungary: an integrated geochemical investigation of mineral phases and glasses. *Lithos* **148**, 71–85. https://doi.org/10.1016/j.lithos.2012.06.009.

Davidson, T. & Tepley, F. J. (1997). Recharge in volcanic systems: evidence from isotope profiles of phenocrysts. *Science* **275**, 826–829. https://doi.org/10.1126/science.275.5301.826.

Davidson, J., Turner, S., Handley, H., Macpherson, C. & Dosseto, A. (2007). Amphibole "sponge" in arc crust? *Geology* **35**, 787–790. https://doi.org/10.1130/G23637A.1.

Defant, M. J. & Drummond, M. S. (1990). Derivation of some modern arc magmas by melting of young subducted lithosphere. *Nature* **347**, 662–665. https://doi.org/10.1038/347662a0.

Defant, M. J. & Drummond, M. S. (1993). Mount St. Helens: potential example of the partial melting of the subducted lithosphere in a volcanic arc. *Geology* **21**, 547–550. https://doi.org/10.1130/0091-7613(1993)021<0547:MSHPEO>2.3.CO;2.

DePaolo, D. J. (1981). Trace element and isotopic effects of combined wallrock assimilation and fractional crystallisation. *Earth and Planetary Science Letters* **53**, 189–202. https://doi.org/10.1016/0012-821X(81)90153-9.

Dohmen, R. & Blundy, J. (2014). A predictive thermodynamic model for element partitioning between plagioclase and melt as a function of pressure, temperature and composition. *American Journal of Science* **314**, 1319–1372. https://doi.org/10.2475/09.2014.04.

Eichelberger, J. C. (1975). Origin of andesite and dacite: evidence of mixing at Glass Mountain in California and at other circum-Pacific volcanoes. *Geological Society of America Bulletin* **86**, 1381–1391. https://doi.org/10.1130/0016-7606(1975)86<1381:OOAADE>2.0.CO;2.

Eichelberger, J. C. (1978). Andesitic volcanism and crustal evolution. *Nature* **275**, 21–27. https://doi.org/10.1038/275021a0.

Eichelberger, J. C., Izbekov, P. E. & Browne, B. L. (2006). Bulk chemical trends at arc volcanoes are not liquid lines of descent. *Lithos* **87**, 135–154. https://doi.org/10.1016/j.lithos.2005.05.006.

Erdmann, S., Martel, C., Pichavant, M. & Kushnir, A. (2014). Amphibole as an archivist of magmatic crystallization conditions: problems, potential, and implications for inferring magma storage prior to the paroxysmal 2010 eruption of mount Merapi, Indonesia. *Contributions to Mineralogy and Petrology* **167**, 1016. https://doi.org/10.1007/s00410-014-1016-4.

Evans, T. M., O'Neill, H. S. C. & Tuff, J. (2008). The influence of melt composition on the partitioning of REEs, Y, Sc, Zr and Al between forsterite and melt in the system CMAS. *Geochimica et Cosmochimica Acta* **72**, 5708–5721. https://doi.org/10.1016/j.gca.2008.09.017.

Folkes, C. B., de Silva, S. L., Bindeman, I. N. & Cas, R. A. F. (2013). Tectonic and climate history influence the geochemistry of large-volume silicic magmas: new δ^{18}O data from the Central Andes with comparison to N America and Kamchatka. *Journal of Volcanology and Geothermal Research* **262**, 90–103. https://doi.org/10.1016/j.jvolgeores.2013.05.014.

Gill, J. B. (1981) *Orogenic Andesites and Plate Tectonics*. Berlin: Springer.

Hammarstrom, J. M. & Zen, E. (1986). Aluminum in hornblende: an empirical igneous geobarometer. *American Mineralogist* **71**, 1297–1313.

Holland, T. J. B. & Blundy, J. D. (1994). Non-ideal interactions in calcic amphiboles and their bearing on amphibole-plagioclase thermometry. *Contributions to Mineralogy and Petrology* **116**, 433–447. https://doi.org/10.1007/BF00310910.

Holtz, F., Sato, H., Lewis, J., Behrens, H. & Nakada, S. (2005). Experimental petrology of the 1991–1995 Unzen dacite, Japan. Part I: phase relations, phase composition and pre-eruptive conditions. *Journal of Petrology* **46**, 319–337. https://doi.org/10.1093/petrology/egh077.

Hoshizumi, H., Ono, K., Mimura, K. & Noda, T. (1988). Geology of the Beppu district. *With Geological Sheet map at 1:50,000* , 131 Geological Survey of Japan (in Japanese with English abstract).

Humphreys, M. C. S., Cooper, G. F., Zhang, J., Loewen, M., Kent, A. J. R., Macpherson, C. G. & Davidson, J. P. (2019). Unravelling the complexity of magma plumbing at Mount St. Helens: a new trace element partitioning scheme for amphibole. *Contributions to Mineralogy and Petrology* **174**, 9. https://doi.org/10.1007/s00410-018-1543-5.

Ishibashi, H., Suwa, Y., Miyoshi, M., Yasuda, A. & Hokanishi, N. (2018). Amphibole-melt disequilibrium in silicic melt of the Aso-4 caldera-forming eruption at Aso volcano, SW Japan. *Earth, Planets and Space* **70**, 137. https://doi.org/10.1186/s40623-018-0907-4.

Itoh, J. (1989). Geology and volcanic activity of the Hime-Shima volcanic group, North Kyushu, Japan. *Bulletin of the Volcanological Society of Japan* **34**, 1–17 (in Japanese with English abstract).

Iveson, A. A., Rowe, M. C., Webster, J. D. & Neill, O. K. (2018). Amphibole-, clinopyroxene- and plagioclase-melt partitioning of trace and economic metals in halogen-bearing rhyodacitic melts. *Journal of Petrology* **59**, 1579–1604. https://doi.org/10.1093/petrology/egy072.

Jochum, K. P., Weis, U., Stoll, B., Kuzmin, D., Yang, Q., Raczek, I., Jacob, D. E., Stracke, A., Birbaum, K., Frick, D. A., Günther, D. & Enzweiler, J. (2011). Determination of reference values for NIST SRM 610-617 glasses following ISO guidelines. *Geostandards and Geoanalytical Research* **35**, 397–429. https://doi.org/10.1111/j.1751-908X.2011.00120.x.

Johnson, M. C. & Rutherford, M. J. (1989). Experimental calibration of the aluminum-in-hornblende geobarometer with application to long Valleycaldera (California) volcanic rocks. *Geology* **17**, 837–841. https://doi.org/10.1130/0091-7613(1989)017<0837:ECOTAI>2.3.CO;2.

Kagami, H., Yuhara, M., Iizumi, S., Tainosho, Y., Owada, M., Ikeda, Y., Okano, O., Ochi, S., Hayama, Y. & Kureki, T. (2000). Continental basalts in the accretionary complexes of the south-West Japan arc: constraints from geochemical and Sr and Nd isotopic data of metadiabase. *The Island Arc* **9**, 3–20. https://doi.org/10.1046/j.1440-1738.2000.00257.x.

Kamei, A., Miyake, Y., Owada, M. & Kimura, J. I. (2009). A pseudo adakite derived from partial melting of tonalitic to granodioritic crust, Kyushu, Southwest Japan arc. *Lithos* **112**, 615–625. https://doi.org/10.1016/j.lithos.2009.05.024.

Kawamoto, T. (1992). Dusty and honeycomb plagioclase: indicators of processes in the Uchino stratified magma chamber, Izu peninsula, Japan. *Journal of Volcanology and Geothermal Research* **49**, 191–208. https://doi.org/10.1016/0377-0273(92)90014-5.

Kawanabe, Y., Hoshizumi, H., Itoh, J. & Yamasaki, S. (2015). Geological map of Kuju volcano. *Geological map of volcanoes* **19**, (in Japanese with English abstract).

Kent, A. J. R. (2014) Preferential eruption of andesitic magmas: Implications for volcanic magma fluxes at convergent margins. In: Gómez-Tuena A., Straub S. M. & Zellmer G. F. (eds) *Orogenic Andesites and Crustal Growth*. London: Geological Society, London, Special Publications, pp.257–280.

Kent, A. J. R., Darr, C., Koleszar, A. M., Salisbury, M. J. & Cooper, K. M. (2010). Preferential eruption of andesitic magmas through recharge filtering. *Nature Geoscience* **3**, 631–636. https://doi.org/10.1038/ngeo924.

Kimura, J. & Nagahashi, Y. (2007). Origin of a voluminous iron-enriched high-K rhyolite magma erupted in the North Japan Alps at 1.75 ma: evidence for upper crustal melting. *Journal of Volcanology and Geothermal Research* **167**, 81–99. https://doi.org/10.1016/j.jvolgeores.2007.02.004.

Kimura, J., Tateno, M. & Osaka, I. (2005). Geology and geochemistry of Karasugasen lava dome, Daisen–Hiruzen volcano group, Southwest Japan. *The Island Arc* **14**, 115–136. https://doi.org/10.1111/j.1440-1738.2005.00461.x.

Kimura, J., Gill, J. B., Kunikiyo, T., Osaka, I., Shimoshioiri, Y., Katakuse, M., Kakubuchi, S., Nagao, T., Furuyama, K., Kamei, A., Kawabata, H., Nakajima, J., van Keken, P. E. & Stern, R. J. (2014). Diverse magmatic effects of subducting a hot slab in SW Japan: results from forward modeling. *Geochemistry, Geophysics, Geosystems* **15**, 691–739. https://doi.org/10.1002/2013GC005132.

Kimura, J., Nagahashi, Y., Satoguchi, Y. & Chang, Q. (2015). Origins of felsic magmas in Japanese subduction zone: geochemical characterizations of tephra from caldera-forming eruptions <5 ma. *Geochemistry, Geophysics, Geosystems* **16**, 2147–2174. https://doi.org/10.1002/2015GC005854.

Kobayashi, T. (1984). Geology of Yufu-Tsurumi volcanoes and their latest eruptions. *The Memories of the Geological Society of Japan* **24**, 93–108 (in Japanese with English abstract).

Koyaguchi, T. (1986). Textural and compositional evidence for magma mixing and its mechanism, Abu volcano group, southwestern Japan. *Contributions to Mineralogy and Petrology* **93**, 33–45. https://doi.org/10.1007/BF00963583.

Kuno, H. (1968). Origin of andesite and its bearing on the island arc structure. *Bulletin Volcanologique* **32**, 141–176. https://doi.org/10.1007/BF02596589.

Leake, B. E. (1968). A catalog of analyzed calciferous and subcalciferous amphiboles together with their nomenclature and associated minerals. *A Catalog of Analyzed Calciferous and Subcalciferous Amphiboles Together with Their Nomenclature and Associated Minerals* **98**, 1–44. https://doi.org/10.1130/SPE98-p1.

Leake, B. E., Woolley, A. R., Arps, C. E. S., Birch, W., Gilbert, M. C., Grice, J. D., Hawthorne, F. C., Kato, A., Kisch, H., Krivovichev, V. G., Linthout, K., Laird, J., Mandarino, J. A., Maresche, W. V., Nickel, E. H., Rock, N. M. S., Schumacher, J. C., Smith, D. C., Stephenson, N. C. N., Ungaretti, L., Whittaker, E. J. W. & Youzhi, G. (1997). Nomenclature of amphiboles: report of the subcommittee on amphiboles of the international mineralogical association, commission on new minerals and mineral names. *The Canadian Mineralogist* **35**, 219–246.

Machida, H. & Arai, F. (2003) *Atlas of tephra in and around Japan*. Tokyo: University of Tokyo Press, (in Japanese).

Mahony, S. H., Wallace, L. M., Miyoshi, M., Villamor, P., Sparks, R. S. J. & Hasenaka, T. (2011). Volcano–tectonic interactions during rapid plate-boundary evolution in the Kyushu region, SW Japan. *Geological Society of America Bulletin* **123**, 2201–2223. https://doi.org/10.1130/B30408.1.

Matsumoto, Y. (1993). Conception of the Beppu-Shimabara graben,its development and problems. *The Memories of the Geological Society of Japan* **41**, 175–192 (in Japanese with English abstract).

Molina, J. F., Moreno, J. A., Castro, A., Rodríguez, C. & Fershtater, G. B. (2015). Calcic amphibole thermobarometry in metamorphic and igneous rocks: new calibrations based on plagioclase/amphibole Al-Si partitioning and amphibole/liquid mg partitioning. *Lithos* **232**, 286–305. https://doi.org/10.1016/j.lithos.2015.06.027.

Morris, P. A. (1995). Slab melting as an explanation of quaternary volcanism and aseismicity in Southwest Japan. *Geology* **23**, 395–398. https://doi.org/10.1130/0091-7613(1995)023<0395:SMAAEO>2.3.CO;2.

Nagasaki, S., Ishibashi, H., Suwa, Y., Yasuda, A., Hokanishi, N., Ohkura, T. & Takemura, K. (2017). Magma reservoir conditions beneath Tsurumi volcano, SW Japan: evidence from amphibole thermobarometry and seismicity. *Lithos* **278-281**, 153–165. https://doi.org/10.1016/j.lithos.2017.01.011.

Ohkura, T., Furukawa, Y., Takemura, K. & Mawatari, H. (2002). Seismic activity in the Beppu graben, Kyushu, Japan. *Institute for Geothermal Research, Graduate School of Science, Kyoto UniversityAnnual Report* FY2002. , 2–4.

Ohta, T. & Aoki, K. (1991). Origin of andesitic magma in Yufu-Tsurumi volcanic group —a binary mixing model. *Journal of Mineralogy, Petrology and Economic Geology* **86**, 1–15(in Japanese with English abstract). https://doi.org/10.2465/ganko.86.1.

Ohta, T., Hasenaka, T. & Fujimaki, H. (1990). Geology and petrography of Yufu-Tsurumi volcano group, Oita prefecture. *Journal of Mineralogy, Petrology and Economic Geology* **85**, 113–129(in Japanese with English abstract). https://doi.org/10.2465/ganko.85.113.

Okada, I., Shibata, T., Ishibashi, H., Sugimoto, T., Yoshikawa, M. & Takemura, K. (2018). Magma generation process of the quaternary Yufu volcano, Northeast Kyushu, Japan: approach from petrological features of amphibole. *Chikyu Monthly/Special* **69**, 160–166 (in Japanese).

Okano, O., Sato, T. & Kagami, H. (2000). Rb–Sr and Sm–Nd isotopic studies of mafic igneous rocks from the Ryoke plutono-metamorphic belt in the Setouchi area, Southwest Japan: implications for the genesis and thermal history. *The Island Arc* **9**, 21–36. https://doi.org/10.1046/j.1440-1738.2000.00258.x.

Osanai, Y., Masao, S. & Kagami, H. (1990). Rb-Sr whole rock isochron ages of granitic rocks from Central Kyushu, Japan. *Memories of the Geological Society of Japan* **42**, 135–150 (in Japanese with English abstract).

Padilla, A. J. & Gualda, G. A. R. (2016). Crystal-melt elemental partitioning in silicic magmatic systems: an example from the peach Spring Tuff high-silica rhyolite, Southwest USA. *Chemical Geology* **440**, 326–344. https://doi.org/10.1016/j.chemgeo.2016.07.004.

Peppard, B. T., Steele, I. M., Davis, A. M., Wallace, P. J. & Anderson, A. T. (2001). Zoned quartz phenocrysts from the rhyolitic bishop Tuff. *American Mineralogist* **86**, 1034–1052. https://doi.org/10.2138/am-2001-8-910.

Perfit, M. R., Gust, A. E., Bence, A. E., Arculus, R. J. & Taylor, S. R. (1980). Chemical characteristics of island-arc basalt: implications for mantle sources. *Chemical Geology* **30**, 227–256. https://doi.org/10.1016/0009-2541(80)90107-2.

Pichavant, M., Costa, F., Burgisser, A., Scaillet, B., Martel, C. & Poussineau, S. (2007). Equilibration scales in silicic to intermediate magmas—implications for experimental studies. *Journal of Petrology* **48**, 1955–1972. https://doi.org/10.1093/petrology/egm045.

Putirka, K. (2016). Amphibole thermometers and barometers for igneous systems and some implications for eruption mechanisms of felsic magmas at arc volcanoes. *American Mineralogist* **101**, 841–858. https://doi.org/10.2138/am-2016-5506.

Reubi, O. & Blundy, J. (2009). A dearth of intermediate melts at subduction zone volcanoes and the petrogenesis of arc andesites. *Nature* **461**, 1269–1273. https://doi.org/10.1038/nature08510.

Ridolfi, F. (2021). Amp-TB2: an updated model for calcic amphibole thermobarometry. *Minerals* **11**, 324. https://doi.org/10.3390/min11030324.

Ridolfi, F. & Renzulli, A. (2012). Calcic amphiboles in calc-alkaline and alkaline magmas: thermobarometric and chemometric empirical equations valid up to 1,130 °C and 2.2 Gpa. *Contributions to Mineralogy and Petrology* **163**, 877–895. https://doi.org/10.1007/s00410-011-0704-6.

Ridolfi, F., Purtini, M., Renzulli, A., Menna, M. & Toulkeridis, T. (2008). The magmatic feeding system of El Reventador volcano (sub-Andean zone, Ecuador) constrained by texture, mineralogy and thermobarometry of the 2002 erupted products. *Journal of Volcanology and Geothermal Research* **176**, 94–106. https://doi.org/10.1016/j.jvolgeores.2008.03.003.

Roedder, E. (1979). Origin and significance of magmatic inclusions. *Bulletin de Minéralogie* **102**, 487–510. https://doi.org/10.3406/bulmi.1979.7299.

Rutherford, M. J. & Devine, J. D. (1988). The may 18, 1980, eruption of Mount St. Helens: 3. Stability and chemistry of amphibole in the magma chamber. *Journal of Geophysical Research* **93**, 11949–11959. https://doi.org/10.1029/JB093iB10p11949.

Saito, G., Kazahaya, K., Shinohara, H., Stimac, J. & Kawanabe, Y. (2001). Variation of volatile concentration in a magma system of Satsuma-Iwojima volcano deduced from melt inclusion analyses. *Journal of Volcanology and Geothermal Research* **108**, 11–31. https://doi.org/10.1016/S0377-0273(00)00276-6.

Sakuyama, M. (1979). Evidence of magma mixing: petrological study of Shirouma-Oike calc-alkaline andesite volcano, Japan. *Journal of Volcanology and Geothermal Research* **5**, 179–208. https://doi.org/10.1016/0377-0273(79)90040-4.

Sakuyama, M. (1981). Petrological study of the Myoko and Kurohime volcanoes, Japan: crystallization sequence and evidence for magma mixing. *Journal of Petrology* **22**, 553–583. https://doi.org/10.1093/petrology/22.4.553.

Sakuyama, M. (1983). Phenocryst assemblages and H_2O content in circum-pacific arc magmas. *Geodynamics of the*

Western Pacific-Indonesian Region **11**, 143–158. https://doi.org/10.1029/GD011p0143.

Schmidt, M. W. (1992). Amphibole composition in tonalite as a function of pressure: an experimental calibration of the Al-in-hornblende barometer. *Contributions to Mineralogy and Petrology* **110**, 304–310. https://doi.org/10.1007/BF00310745.

Shibata, T., Yoshikawa, M., Itoh, J., Ujike, O., Miyoshi, M. & Takemura, K. (2014) Along-arc geochemical variations in Quaternary magmas of northern Kyushu Island, Japan. In: Gómez-Tuena A., Straub S. M. & Zellmer G. F. (eds) *Orogenic Andesites and Crustal Growth*. London: Geological Society, London, Special Publications, pp.15–29.

Shimizu, K., Liang, Y., Sun, C., Jackson, C. R. M. & Saal, A. (2017). Parameterized lattice strain models for REE partitioning between amphibole and silicate melt. *American Mineralogist* **102**, 2254–2267. https://doi.org/10.2138/am-2017-6110.

Singer, B. S., Dungan, M. A. & Layne, G. D. (1995). Textures and Sr, Ba, mg, Fe, K, and Ti compositional profiles in volcanic plagioclase: clues to the dynamics of calc-alkaline magma chambers. *American Mineralogist* **80**, 776–798. https://doi.org/10.2138/am-1995-7-815.

Sisson, T. W., Ratajeski, K., Hankins, W. B. & Glazner, A. F. (2005). Voluminous granitic magmas from common basaltic sources. *Contributions to Mineralogy and Petrology* **148**, 635–661. https://doi.org/10.1007/s00410-004-0632-9.

Stern, R. J. (1979). On the origin of andesite in the northern Mariana Island arc: implications from Agrigan. *Contributions to Mineralogy and Petrology* **68**, 207–219. https://doi.org/10.1007/BF00371901.

Sugimoto, T., Shibata, T., Yoshikawa, M. & Takemura, K. (2006). Sr–Nd–Pb isotopic and major and trace element compositions of the Yufu–Tsurumi volcanic rocks: implications for the mama genesis of the Yufu–Tsurumi volcanoes, Northeast Kyushu, Japan. *Journal of Mineralogical and Petrological Sciences* **101**, 270–275. https://doi.org/10.2465/jmps.101.270.

Sun, S. S. & McDonough, W. F. (1989) Chemical and isotopic systematics of oceanic basalts: Implications for mantle composition and processes. In: Saunders A. D. & Norry M. J. (eds) *Magmatism in the Ocean Basins*. London: Geological Society, London, Special Publications, pp.313–345.

Takagi, T., Naito, K. & Kamei, A. (2010). Petrographic contrast between ilmenite- and magnetite-series gabbroids in the Ryoke and san-in belts, southwestern Japan arc. *Journal of Mineralogical and Petrological Sciences* **105**, 194–214. https://doi.org/10.2465/jmps.081208.

Tepley, F. J., Davidson, J. P., Tilling, R. I. & Arth, J. G. (2000). Magma mixing, recharge and eruption histories recorded in plagioclase Phenocrysts from El Chichón volcano, Mexico. *Journal of Petrology* **41**, 1397–1411. https://doi.org/10.1093/petrology/41.9.1397.

Tiepolo, M., Oberti, R., Zanetti, A., Vannucci, R. & Foley, S. F. (2007) Trace-element partitioning between amphibole and Silicate melt. In: Hawthorne F. C., Oberti R., Della V. G. & Mottana A. (eds) *Amphiboles: Crystal Chemistry, Occurrence, and Health Issues*. Chantilly, VA: Reviews in Mineralogy and Geochemistry, pp.417–452.

Tiepolo, M., Tribuzio, R. & Langone, A. (2011). High-mg andesite petrogenesis by amphibole crystallization and ultramafic crust assimilation: evidence from Adamello hornblendites (Central Alps, Italy). *Journal of Petrology* **52**, 1011–1045. https://doi.org/10.1093/petrology/egr016.

Tiepolo, M., Langone, A., Morishita, T. & Yuhara, M. (2012). On the recycling of amphibole-rich ultramafic intrusive rocks in the arc crust: evidence from Shikanoshima Island (Kyushu, Japan). *Journal of Petrology* **53**, 1255–1285. https://doi.org/10.1093/petrology/egs016.

Tsuchiyama, A. (1986). Dissolution kinetics of plagioclase in the melt of the system diopside-albite-anorthite, and origin of dusty plagioclase in andesites. *Contributions to Mineralogy and Petrology* **89**, 1–16.

Turner, S. J., Izbekov, P. & Langmuir, C. (2013). The magma plumbing system of Bezymianny volcano: insights from a 54 year time series of trace element whole-rock geochemistry and amphibole compositions. *Journal of Volcanology and Geothermal Research* **263**, 108–121. https://doi.org/10.1016/j.jvolgeores.2012.12.014.

Wallis, S. R., Yamaoka, K., Mori, H., Ishiwatari, A., Miyazaki, K. & Ueda, H. (2020). The basement geology of Japan from a to Z. *The Island Arc* **29**, 1. https://doi.org/10.1111/iar.12339.

Wanke, M., Karakas, O. & Bachmann, O. (2019). The genesis of arc dacites: the case of Mount St. Helens, WA. *Contributions to Mineralogy and Petrology* **174**, 7. https://doi.org/10.1007/s00410-018-1542-6.

Werts, K., Barnes, C. G., Memeti, V., Ratschbacher, B., Williams, D. & Paterson, S. R. (2020). Hornblende as a tool for assessing mineral-melt equilibrium and recognition of crystal accumulation. *American Mineralogist* **105**, 77–91. https://doi.org/10.2138/am-2020-6972.

Wieser, P. E., Petrelli, M., Lubbers, J., Wieser, E., Özaydın, S., Kent, A. J. R. & Till, C. B. (2022). Thermobar: an open-source Python3 tool for thermobarometry and hygrometry. *Volcanica* **5**, 349–384. https://doi.org/10.30909/vol.05.02.349384.

Wieser, P. E., Gleeson, M. L. M., Matthews, S., DeVitre, C. & Gazel, E. (2023). Determining the pressure – temperature – composition (P-T-X) conditions of magma storage. *Earth Arxiv* . doi.org/10.31223/X50M44.

Wood, D. A., Joron, J. L. & Treuil, M. (1979). A re-appraisal of use of trace elements to classify and discriminate between magma series erupted in different tectonic setting. *Earth and Planetary Science Letters* **45**, 326–336. https://doi.org/10.1016/0012-821X(79)90133-X.

Zhang, J., Hamphreys, M. C. S., Cooper, G. F., Davidson, J. P. & Macpherson, C. G. (2017). Magma mush chemistry at subduction zones, revealed by new melt major element inversion from calcic amphiboles. *American Mineralogist* **102**, 1353–1367. https://doi.org/10.2138/am-2017-5928.